

AN EFFICIENT FRAMEWORK FOR CREDITING DATA CONTRIBUTORS OF DIFFUSION MODELS

Anonymous authors

Paper under double-blind review

ABSTRACT

As diffusion models are deployed in real-world settings, and their performance is driven by training data, appraising the contribution of data contributors is crucial to creating incentives for sharing quality data and to implementing policies for data compensation. Depending on the use case, model performance corresponds to various global properties of the distribution learned by a diffusion model (e.g., overall aesthetic quality). Hence, here we address the problem of attributing global properties of diffusion models to data contributors. The Shapley value provides a principled approach to valuation by uniquely satisfying game-theoretic axioms of fairness. However, estimating Shapley values for diffusion models is computationally impractical because it requires retraining on many training data subsets corresponding to different contributors and rerunning inference. We introduce a method to efficiently retrain and rerun inference for Shapley value estimation, by leveraging model pruning and fine-tuning. We evaluate the utility of our method with three use cases: (i) image quality for a DDPM trained on a CIFAR dataset, (ii) demographic diversity for an LDM trained on CelebA-HQ, and (iii) aesthetic quality for a Stable Diffusion model LoRA-finetuned on Post-Impressionist artworks. Our results empirically demonstrate that our framework can identify important data contributors across models’ global properties, outperforming existing attribution methods for diffusion models.

1 INTRODUCTION

Diffusion models have demonstrated impressive performance on image generation (Ho et al., 2020; Song et al., 2020b), with models such as Dall-E 2 (Ramesh et al., 2022) and Stable Diffusion (Rombach et al., 2022) showing versatile utilities and enabling downstream applications via customization (Hu et al., 2021; Ruiz et al., 2023). A key driver for the performance of diffusion models is the data used for training and fine-tuning. The data for commercial diffusion models are often scraped from the internet (Schuhmann et al., 2022), raising concerns about credit attribution for those who created the data in the first place (e.g., artists and their artworks) (Jiang et al., 2023). Additionally, as labor is required to label and curate data to further improve model performance, demands for data labeling platforms have risen, with workers often underpaid (Widder et al., 2023; Wong, 2023). To create incentives for sharing quality data and implement policies for data compensation, a pressing question arises: *How do we fairly credit data contributors of diffusion models?*

Data attribution, which aims to trace machine learning model behaviors back to training data, has the potential to address the above question. Indeed, in the context of supervised learning, several works have proposed methods for valuating the contribution of individual datum to model performance such as accuracy (Ghorbani & Zou, 2019; Kwon & Zou, 2021; Wang & Jia, 2023). Some recent work has developed data attribution methods for diffusion models (Dai & Gifford, 2023; Georgiev et al., 2023; Wang et al., 2023a; Zheng et al., 2023). However, two gaps remain when applying these recent methods to credit data contributors of diffusion models. First, these methods focus on *local* properties related to the generation of a given image. For example, Zheng et al. (2023) showcase their method D-TRAK to study the changes in pixel values of particular generated images. In contrast, the performance of diffusion models is evaluated based on *global* properties of the learned generative distributions. For example, the demographic diversity of generated images can be considered a global property for evaluation (Luccioni et al., 2023). Second, existing attribution methods for diffusion models consider the contribution of each training datum instead of each data contributor, but a

contributor can provide multiple data points. One reasonable approach is to aggregate the valuations of data provided by a contributor as the contributor’s total contribution. However, previous work has shown this approach to incur errors between the aggregated and actual contribution (Koh et al., 2019). Here, we aim to address these two gaps by attributing global properties of diffusion models to data contributors.

Attribution methods based on cooperative game theory are particularly desirable because of their axiomatic justification. Specifically, the Shapley value provides a principled approach to fairly distribute credit among contributors, since it is the unique notion that satisfies game-theoretic axioms for equitable valuation (Ghorbani & Zou, 2019; Shapley, 1953). Briefly, the Shapley value assesses each contributor based on the average gain incurred by adding the contributor’s data to different contributor combinations. To estimate the Shapley values for data contributors in our setting, we need to (i) retrain diffusion models on data subsets corresponding to different combinations of contributors; and (ii) measure global properties of the retrained models by rerunning inference. However, training a diffusion model can take hundreds of GPU days, and inference can also be expensive (e.g., approximately 5 GPU days to generate 50,000 images for image quality metrics) (Dhariwal & Nichol, 2021). Therefore, estimating Shapley values with vanilla retraining and inference is computationally impractical. Here, we propose to efficiently approximate retraining and inference on retrained models through model pruning and fine-tuning, providing a framework that enables Shapley value estimation (Figure 1).

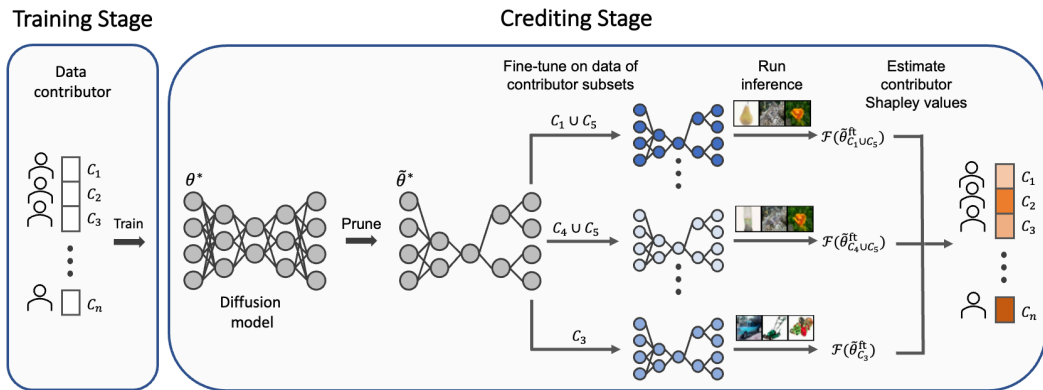


Figure 1: Schematic overview of our proposed framework, where θ^* denotes a trained diffusion model for which we aim to credit data contributors, and $\tilde{\theta}^*$ denotes the pruned model that approximates θ^* . After fine-tuning the pruned model on data corresponding to various subsets of contributors, denoted as $\tilde{\theta}^{ft}$, and rerunning inference; global model properties (\mathcal{F}) are measured to estimate the Shapley value for each data contributor.

Related work. Data attribution methods for diffusion models have been developed by recent work. Some methods require models be trained with specialized paradigms. For example, to assess the importance for a training sample, Dai & Gifford (2023) first train an ensemble of diffusion models on data splits, followed by ablating models trained on splits containing the specific sample. Wang et al. (2023a) evaluate data attribution for text-to-image models by customizing a pretrained model toward an exemplar style. In contrast, other methods can be applied to already trained models in a post hoc manner. For example, the TRAK framework has been adapted to find important training data for intermediate latents along a generative process (Georgiev et al., 2023), while Zheng et al. (2023) introduce empirical approaches that improve the performance of TRAK for diffusion models. All these methods attribute local model properties to each individual datum, whereas our work focuses on attributing global model properties to each data contributor.

Contributions. (1) To our knowledge, we are the first to investigate how to attribute global properties of diffusion models to data contributors. (2) We propose a framework that efficiently approximates retraining and rerunning inference for diffusion models, enabling the estimation of Shapley values for data contributors. (3) We empirically demonstrate that our framework outperforms existing attribution methods across three datasets, model architectures, and global properties.

2 PRELIMINARIES

This section provides an overview for diffusion models, attributing global model properties to data contributors, and existing attribution methods for diffusion models.

2.1 DIFFUSION MODELS

Our research primarily focuses on discrete-time diffusion models, specifically denoising diffusion probabilistic models (DDPMs) (Ho et al., 2020) and latent diffusion models (LDMs) (Rombach et al., 2022). Generally, diffusion models are trained to approximate a data distribution $q(\mathbf{x}_0)$. To perform learning, a training sample $\mathbf{x}_0 \sim q(\mathbf{x}_0)$ is sequentially corrupted by additive noise (Ho et al., 2020). This procedure is called the *forward process* and is defined by $q(\mathbf{x}_t|\mathbf{x}_{t-1}) := \mathcal{N}(\mathbf{x}_t; \sqrt{1 - \beta_t}\mathbf{x}_{t-1}, \beta_t\mathbf{I})$, for $t = 1, \dots, T$, where $\{\beta_t\}_{t=1}^T$ corresponds to a variance schedule. Notably, the forward process allows sampling of \mathbf{x}_t at any time step t from \mathbf{x}_0 , with the closed form $q(\mathbf{x}_t|\mathbf{x}_0) = \mathcal{N}(\mathbf{x}_t; \sqrt{\bar{\alpha}_t}\mathbf{x}_0, (1 - \bar{\alpha}_t)\mathbf{I})$, where $\alpha_t := 1 - \beta_t$ and $\bar{\alpha}_t := \prod_{s=1}^t \alpha_s$. Then, a diffusion model learns to denoise $\mathbf{x}_{1:T}$, following the *reverse process* defined by $p_\theta(\mathbf{x}_{t-1}|\mathbf{x}_t) := \mathcal{N}(\mathbf{x}_{t-1}; \mu_\theta(\mathbf{x}_t, t), \sigma_t^2\mathbf{I})$, where $\theta \in \mathbb{R}^d$ is the model parameters, and σ_t corresponds to some sampling schedule (Karras et al., 2022). Instead of modeling the conditional means μ_θ , it is standard to predict the added noises with a neural network ϵ_θ using the reparameterization trick. The training objective corresponds to a variational bound and is formulated as

$$\mathcal{L}_{\text{Simple}}(\mathbf{x}; \theta) = \mathbb{E}_{t, \epsilon} \left[\|\epsilon - \epsilon_\theta(\sqrt{\bar{\alpha}_t}\mathbf{x} + \sqrt{1 - \bar{\alpha}_t}\epsilon, t)\|_2^2 \right] \quad (1)$$

Once a diffusion model has been trained, a new image can be generated by sampling an initial noise $\mathbf{x}_T \sim \mathcal{N}(\mathbf{0}, \mathbf{I})$ and iteratively applying ϵ_θ at each step $t = T, \dots, 1$ for denoising.

2.2 ATTRIBUTING GLOBAL MODEL PROPERTIES TO DATA CONTRIBUTORS

To gain a comprehensive understanding of machine learning models, it is often beneficial to study global model properties (Covert et al., 2020), which assess the model’s performance across samples, rather than focusing on individual outputs. For example, in the setting of supervised learning, global model property can be test accuracy. In the context of generative models, it can be a quality metric for generated samples. For example, in image generation, the global model property of interest can be the Inception Score (Goodfellow et al., 2014) or FID (Heusel et al., 2017). More formally, a global model property for generative models is defined by any application-specific function $\mathcal{F} : \Theta \rightarrow \mathbb{R}$, which maps a generative model to a scalar value, thereby quantifying the overall distribution learned by the model. Building on this, we introduce the problem of attributing global model properties to data contributors. The goal of contributor attribution is to identify important groups of training data for a model’s global properties, where each group of data is provided by a contributor. More formally, we have the following definition.

Definition 1. (*Contributor attribution*) Consider n contributors of training samples $\mathcal{D} = \{\mathcal{C}_1, \mathcal{C}_2, \dots, \mathcal{C}_n\}$, with the i th contributor providing a set of data points denoted as \mathcal{C}_i , and a global model property function \mathcal{F} . A contributor attribution method is a function $\tau(\mathcal{F}, \{\mathcal{C}_i\}_{i=1}^n)$ that assigns scores to all contributors to indicate each contributor’s importance to the global model property \mathcal{F} .

2.3 EXISTING ATTRIBUTION METHODS FOR DIFFUSION MODELS

In the context of diffusion models, recent work has focused on attributing local model properties to each datum by adapting the TRAK framework (Park et al., 2023), such as D-TRAK (Zheng et al., 2023) and Journey-TRAK (Georgiev et al., 2023). Formally, let \mathcal{X} denote the input space and Θ the parameter space of a diffusion model. Suppose there are N training data points $\{\mathbf{x}^{(1)}, \mathbf{x}^{(2)}, \dots, \mathbf{x}^{(N)}\}$, and $\tilde{\mathbf{x}}$ is the generated image of interest for local attribution. Given a loss function $\mathcal{L} : \mathcal{X} \times \Theta \rightarrow \mathbb{R}$, a local model property $f : \mathcal{X} \times \Theta \rightarrow \mathbb{R}$, and models $\{\theta_s^*\}_{s=1}^S$ trained on S data subsets¹, TRAK for diffusion models is defined as:

$$\frac{1}{S} \sum_{s=1}^S \Phi_s (\Phi_s^\top \Phi_s + \lambda I)^{-1} \gamma_s(\tilde{\mathbf{x}}), \text{ and} \quad (2)$$

¹In practice, we consider the computationally efficient retraining-free setting by Zheng et al. (2023). That is, $S = 1$, and $\theta_1^* = \theta^*$ is the original model trained on the entire dataset.

$$\Phi_s = [\phi_s(\mathbf{x}^{(1)}), \dots, \phi_s(\mathbf{x}^{(N)})]^\top, \quad (3)$$

where $\phi_s(\mathbf{x}) = \mathcal{P}_s^\top \nabla_{\theta} \mathcal{L}(\mathbf{x}; \theta_s^*)$, $\gamma_s(\mathbf{x}) = \mathcal{P}_s^\top \nabla_{\theta} f(\mathbf{x}; \theta_s^*)$, \mathcal{P}_s is a random projection matrix, and λI serves for numerical stability and regularization. More details on Journey-TRAK (Georgiev et al., 2023) and D-TRAK (Zheng et al., 2023) are in Appendix E.

3 CREDITING DATA CONTRIBUTORS OF DIFFUSION MODELS USING THE SHAPLEY VALUE

Here, we motivate the use of the Shapley value for crediting data contributors of diffusion models. While estimating Shapley values for diffusion models require computationally expensive retraining and inference, we propose to address the computational challenge with model pruning and fine-tuning.

3.1 THE SHAPLEY VALUE FOR CONTRIBUTOR ATTRIBUTION

The Shapley value was developed in cooperative game theory to fairly attribute credit in coalition games (Shapley, 1953). In the context of contributor attribution, for training data with n contributors, the Shapley value attributed to the i th contributor is defined as:

$$\beta_i = \frac{1}{n} \sum_{S \subseteq D \setminus \mathcal{C}_i} \binom{n-1}{|S|}^{-1} (\mathcal{F}(\theta_{S \cup \mathcal{C}_i}^*) - \mathcal{F}(\theta_S^*)) \quad (4)$$

where $\theta_{S \cup \mathcal{C}_i}^*$ and θ_S^* are models trained on the subsets $S \cup \mathcal{C}_i$ and S , respectively. The Shapley value appraises each contributor’s contribution based on the weighted *marginal contribution*, $\mathcal{F}(\theta_{S \cup \mathcal{C}_i}^*) - \mathcal{F}(\theta_S^*)$. It satisfies axioms desirable for equitable attribution, including *linearity*, *dummy player*, *symmetry*, and *efficiency* (see Ghorbani & Zou (2019) for a succinct summary). There are arguments that the efficiency axiom, $\sum_{i=1}^n \beta_i = \mathcal{F}(\theta^*) - \mathcal{F}(\theta_\emptyset)$, where θ^* denotes the model trained on the entire dataset, and θ_\emptyset denotes the model without training, may not always be essential in use cases where the primary goal is to remove detrimental data points (Wang & Jia, 2023). In that setting, ranking is more important than exact attribution values. However, in the context of diffusion models, particularly in applications involving monetary or credit allocation related to model performance, having the total attribution matches the model utility can directly quantify reward for each contributor.

Despite its advantages, evaluating the *exact* Shapley value is challenging as it involves retraining 2^n (all possible subsets) models and computing their corresponding model properties. Fortunately, many sampling-based estimators for Shapley values have been developed (Lundberg & Lee, 2017; Ghorbani & Zou, 2019; Štrumbelj & Kononenko, 2010). In particular, we adopt KernelSHAP in the feature attribution literature for contributor attribution, by solving a weighted least squares problem with sampling (Lundberg & Lee, 2017; Covert & Lee, 2021):

$$\hat{\beta} = \min_{\beta_0, \dots, \beta_n} \frac{1}{M} \sum_{j=1}^M \left[\mathcal{F}(\theta_\emptyset) + \mathbf{1}_{S_j}^\top \beta - \mathcal{F}(\theta_{S_j}^*) \right]^2 \quad \text{s.t.} \quad \mathbf{1}^\top \beta = \mathcal{F}(\theta^*) - \mathcal{F}(\theta_\emptyset) \quad (5)$$

where S_j is sampled following the distribution $\mu(S) \propto \frac{n-1}{\binom{n}{|S|} |S| (n-|S|)}$ for $1 < \mathbf{1}_S^\top \beta < n$, and $\mathbf{1}_S$ is an indicator vector representing the presence of contributors in S . By solving the least squares problem with the constraint, a closed-form solution can be derived (Covert & Lee, 2021). The obtained parameters $\hat{\beta}_1, \dots, \hat{\beta}_n$ are the contributor attribution scores.

3.2 SPEED UP RETRAINING AND INFERENCE WITH SPARSIFIED FINE-TUNING

Although using the Shapley value for contributor attribution is well motivated, and existing sampling approach can be used, the main challenge is in computing $\mathcal{F}(\theta_{S_j}^*)$. First, a diffusion model needs to be trained again from random initialization on the subset S_j to obtain $\theta_{S_j}^*$. Then inference needs to be rerun on the retrained model $\theta_{S_j}^*$ to measure $\mathcal{F}(\theta_{S_j}^*)$. For diffusion models, both retraining and rerunning inference can take multiple GPU days (Dhariwal & Nichol, 2021), making the estimator in Equation (5) computationally impractical.

To address this computational challenge, we propose to speed up retraining and rerunning inference with *sparsified fine-tuning* (Figure 1). Sparsified fine-tuning enhances the efficiency of both retraining and inference, by reducing the number of model parameters through pruning (Jia et al., 2023). Specifically, θ^* is pruned and initially fine-tuned on the full dataset \mathcal{D} to obtain a performant pruned model $\tilde{\theta}^*$ that approximates θ^* . To furthermore improve the retraining efficiency, $\tilde{\theta}^*$ is fine-tuned on each subset S_j for k steps to obtain $\tilde{\theta}_{S_j,k}^{\text{ft}}$, instead of retraining the pruned model on S_j from random initialization. The diffusion loss objective used to train the original model θ^* is used for all fine-tuning. Overall, sparsified fine-tuning aims to efficiently achieve

$$\mathcal{F}(\tilde{\theta}_{S_j,k}^{\text{ft}}) \text{ (sparsified fine-tuning)} \approx \mathcal{F}(\theta_{S_j}^*) \text{ (retraining full model from scratch)}. \quad (6)$$

In other words, under the same computational budget and compared to retaining the full model from scratch, sparsified fine-tuning can increase the number of sampled subsets S_j for estimating Shapley values, thus making feasible a framework for crediting data contributors of diffusion models.

In practice, computing $\mathcal{F}(\theta)$ requires sampling N initial noises $\mathbf{x}_T^{(r)} \sim \mathcal{N}(\mathbf{0}, \mathbf{I})$, for $r = 1, \dots, N$, denoising those noises into generated samples with the denoising network ϵ_θ , and computing some quantity over the generated samples (e.g., FID). Hence, to formally analyze the approximation in Equation (6), we consider the expected error² $\mathbb{E}_{\{\mathbf{x}_T^{(r)}\}_{r=1}^N} [|\mathcal{F}(\tilde{\theta}_{S_j,k}^{\text{ft}}) - \mathcal{F}(\theta_{S_j}^*)|]$. For notational ease, the dependency of \mathcal{F} on $\{\mathbf{x}_T^{(r)}\}_{r=1}^N$ is omitted, and all expectations are taken with respect to $\{\mathbf{x}_T^{(r)}\}_{r=1}^N$ for the rest of the paper unless otherwise noted. We then have the following proposition to formalize the intuition behind Equation (6).

Proposition 1. *Suppose an objective function $\ell : \mathbb{R}^d \mapsto \mathbb{R}$ on the data provided by a given subset of data contributors S is convex and differentiable, and that its gradient is Lipschitz-continuous with some constant $L > 0$, i.e.*

$$\|\nabla \ell(\theta_1) - \nabla \ell(\theta_2)\|_2 \leq L \|\theta_1 - \theta_2\|_2$$

for any $\theta_1, \theta_2 \in \mathbb{R}^d$. Let $\tilde{\theta}_{S,k}^{\text{ft}}$ denote a pruned model after k fine-tuning steps on the given subset S with learning rate $\alpha \leq 1/L$, $\tilde{\theta}_S^*$ the optimal pruned model trained on S with the same sparsity structure as $\tilde{\theta}_{S,k}^{\text{ft}}$, and θ_S^* the optimal full-parameter model trained on S . Furthermore, assume that $\mathbb{E}[|\mathcal{F}(\tilde{\theta}_S^*) - \mathcal{F}(\theta_S^*)|] \leq B$ for some constant B . Then the expected error $\mathbb{E}[|\mathcal{F}(\tilde{\theta}_{S,k}^{\text{ft}}) - \mathcal{F}(\theta_S^*)|] \leq B$ as $k \rightarrow \infty$.

The proof is in Appendix A. The assumption that ℓ is convex and differentiable with Lipschitz-continuous gradient is a standard setting for the theoretical analysis of approximating retraining with fine-tuning, instantiated as a quadratic objective³ in Golatkar et al. (2020) and Georgiev et al. (2024). The assumption that $\mathbb{E}[|\mathcal{F}(\tilde{\theta}_S^*) - \mathcal{F}(\theta_S^*)|] \leq B$ corresponds to the *lottery ticket hypothesis* that a sparser neural network can approximate the performance of a dense, full-parameter network (Frankle & Carbin, 2018), which has been shown to hold for diffusion models (Fang et al., 2023). The main takeaway from Proposition 1 is that more steps of sparsified fine-tuning should lead to a bounded approximation error between $\mathcal{F}(\tilde{\theta}_{S_j,k}^{\text{ft}})$ and $\mathcal{F}(\theta_{S_j}^*)$ in Equation (6). We further relate Proposition 1 to the expected error in Shapley values with the following proposition.

Proposition 2. *Let $\tilde{\beta}_k^{\text{ft}} \in \mathbb{R}^n$ be the Shapley values for the data contributors evaluated with $\{\mathcal{F}(\tilde{\theta}_{S,k}^{\text{ft}})\}_{S \in 2^{\mathcal{D}}}$, and $\beta^* \in \mathbb{R}^n$ the Shapley values evaluated with $\{\mathcal{F}(\theta_S^*)\}_{S \in 2^{\mathcal{D}}}$. Suppose the assumptions on ℓ in Proposition 1 hold for all subsets of data contributors. Furthermore, assume that $\mathbb{E}[\max_{S \in 2^{\mathcal{D}}} |\mathcal{F}(\tilde{\theta}_S^*) - \mathcal{F}(\theta_S^*)|] \leq C$. Then $\mathbb{E}[\|\tilde{\beta}_k^{\text{ft}} - \beta^*\|_2] \leq 2\sqrt{n}C$ as $k \rightarrow \infty$.*

The proof is in Appendix A. The assumption that convexity, differentiability, and the Lipschitz continuity of gradient hold for all subsets is implied by the standard setting of a quadratic loss⁴, as in

²We consider the setting where the same $\{\mathbf{x}_T^{(r)}\}_{r=1}^N$ are inputs for both $\epsilon_{\tilde{\theta}_{S_j,k}^{\text{ft}}}$ and $\epsilon_{\theta_{S_j}^*}$ to represent the use case of generating samples with the same random seed across multiple inference runs.

³A quadratic objective has the form $\ell(\theta) = (\theta - B)^\top A(\theta - B)$, with Lipschitz-continuous gradient such that $\|\nabla \ell(\theta_1) - \nabla \ell(\theta_2)\|_2 \leq 2\sigma_{\max}(A) \cdot \|\theta_1 - \theta_2\|_2$, where $\sigma_{\max}(A)$ is the maximum singular value of A .

⁴A Lipschitz constant applicable across all subsets can be defined as $\max_{S \in 2^{\mathcal{D}}} \sigma_{\max}(A_S)$, where A_S is defined by the subset S . For example, in linear regression, $A_S = X_S^\top X_S$, where X_S denotes the feature matrix contributed by the data contributors in S .

270 Golatkar et al. (2020) and Georgiev et al. (2024). The key takeaway is that the Shapley value error
 271 is bounded with more steps of sparsified fine-tuning. Finally, we note that both Proposition 1 and
 272 Proposition 2 are asymptotic results, and that Proposition 2 is based on exact Shapley values. We
 273 leave theoretical results incorporating finite-step bounds and Shapley value estimation for future
 274 work. Nevertheless, we verify the insights from our theoretical results under empirical settings for
 275 diffusion models in Appendix D.

277 4 EXPERIMENTS

278 In this section, we compare our approach with existing attribution methods across three settings. We
 279 employ two metrics for evaluation: linear datamodeling score (LDS) and counterfactual analysis. Our
 280 results demonstrate that our method outperforms existing attribution methods for diffusion models.
 281
 282

283 4.1 DATASETS AND CONTRIBUTORS

284 Datasets used for our experiments include CIFAR-20, a subset of CIFAR-100 with 20 contributors,
 285 one per class, as described in Krizhevsky et al. (2009); CelebA-HQ, with 50 celebrity identities as
 286 contributors; and ArtBench (Post-Impressionism), with 258 artists as contributors. More details about
 287 datasets and contributors can be found in Appendix B.
 288
 289

290 4.2 EXPERIMENT SETTINGS

291 **Model training.** For CIFAR-20, we follow the original implementation of the unconditional DDPM
 292 (Ho et al., 2020) where the model has 35.7M parameters. For CelebA-HQ, we follow the implemen-
 293 tation of LDM (Rombach et al., 2022) with 274M parameters and a pre-trained VQ-VAE (Razavi
 294 et al., 2019). For ArtBench (Post-Impressionism), a Stable Diffusion model (Rombach et al., 2022) is
 295 fine-tuned using LoRA (Hu et al., 2021) with rank = 256, corresponding to 5.1M LoRA parameters.
 296 The prompt for the Stable Diffusion model is set to "*a Post-Impressionist painting*" for each image.
 297 Please refer to Appendix C for more details about model training and inference.
 298

299 **Sparsified fine-tuning.** Magnitude-based pruning (Han et al., 2015) is used to remove model weights
 300 according to their magnitudes, resulting in sparse diffusion models with reduced parameters: from
 301 35.7M to 19.8M for CIFAR-20 at a pruning ratio of 0.3, from 274M to 70.9M for CelebA-HQ at
 302 a ratio of 0.5, and from 5.1M to 2.6M for ArtBench (Post-Impressionism) at a ratio of 0.5. To
 303 estimate Shapley values, the pruned models are fine-tuned on data subsets corresponding to different
 304 contributor combinations, with 1,000 steps, 500 steps, and 200 steps for CIFAR-20, CelebA-HQ, and
 305 ArtBench (Post-Impressionism), respectively.
 306

307 **Global model properties.** For CIFAR-20, we aim to study the contribution of each labeler. As
 308 each labeler is tasked to filter out noisy samples in each class (Krizhevsky et al., 2009), high-quality
 309 labeling should ensure that generated images are well separated with respect to image classes.
 310 Therefore, for the global model property, we choose the Inception Score (Salimans et al., 2016):
 311

$$312 \text{IS} = \exp(\mathbb{E}_{\mathbf{x}}[\text{KL}(p(y|\mathbf{x})||p(y))]), \quad (7)$$

313 where $p(y)$ represents the marginal class distribution over the generated data and $p(y|\mathbf{x})$ represents
 314 the conditional class distribution given a generated image \mathbf{x} .

315 For CelebA-HQ, our goal is to investigate how individual celebrities contribute to the demographic
 316 diversity of the model. Following Luccioni et al. (2023), we measure diversity using entropy:

$$317 \mathcal{H} = - \sum_{k=1}^K p_k \log(p_k), \quad (8)$$

318 where p_k is the proportion of generated samples in the k th demographic cluster. We generate images
 319 using the full model and extract their embeddings with BLIP-VQA (Li et al., 2022) to create 20
 320 reference clusters. Subsequently, we assign these reference clusters to images generated from various
 321 retrained models to calculate the entropy.
 322
 323

For ArtBench (Post-Impressionism), we consider the use case where images are generated and the most aesthetically pleasing ones are kept. We simulate this use case by computing aesthetic scores⁵ for 50 generated images and considering the 90th percentile as the global model property.

More details about these global model properties are in Appendix B.

4.3 BASELINE METHODS

We mainly categorize baseline attribution methods into three categories⁶: (i) similarity-based methods (e.g., pixel similarity between the generated and training images); (ii) leave-one-out (LOO) and its approximate variants such as the influence functions (Koh & Liang, 2017) and TRAK-based methods (Park et al., 2023); and (iii) application-specific metrics such as the aesthetic score of each training image for ArtBench (Post-Impressionism). Because retraining diffusion models is computationally expensive, gradients are computed using the original model θ^* for TRAK-based methods, as done in Zheng et al. (2023). Local attribution scores are averaged for the images generated by the original model and used for computing global model properties. To aggregate datum-level attributions, the sum of attributions corresponding to each contributor is taken for the influence functions and TRAK-based methods, since this is the principled aggregation (Koh et al., 2019). For similarity-based and application-specific methods, datum-level attribution scores are aggregated for contributor attribution by taking either the average or maximum. More details about baseline methods can be found in Appendix E.

4.4 EVALUATING THE PERFORMANCE OF CONTRIBUTOR ATTRIBUTION

Linear datamodeling score (LDS). From Definition 1, for a given subset of contributors $S \subseteq \mathcal{D}$, where $\mathcal{D} = \{C_1, \dots, C_n\}$, we can define an additive datamodel of global properties based on a given set of attribution scores τ for the contributors:

$$g(S, \tau) = \sum_{i: C_i \in S} \tau_i. \quad (9)$$

Therefore, the evaluation for an attribution method τ can be constructed as follows: (Linear datamodeling score) Contributor attribution performance is measured using the linear datamodeling score (LDS) (Ilyas et al., 2022), which evaluates an attribution method by comparing predicted model properties based on the additive datamodel against actual retrained model properties. Let S_1, \dots, S_B be randomly sampled subsets of \mathcal{D} , each of size $\alpha \cdot n$ for some $\alpha \in (0, 1)$. The LDS for a contributor attribution score $\tau \in \mathbb{R}^n$ is defined as

$$LDS = \rho(\{\mathcal{F}(\theta_{S_b}^*)\}_{b=1}^B, \{g(S_b, \tau)\}_{b=1}^B), \text{ where } S_b \sim \text{Uniform}\{S \subset \mathcal{D} : |S| = \alpha \cdot n\}, \quad (10)$$

where ρ is the Spearman rank correlation (Spearman, 1961), and $\theta_{S_b}^*$ denotes a model retrained from scratch with the contributor subset S_b .

We evaluate the LDS using 100 held-out subsets S_b , each sampled from the datamodel distribution with $\alpha = 0.25, 0.5, 0.75$ for each dataset. We report the LDS means and 95% confidence intervals across three independent sets of $\{S_b\}_{b=1}^{100}$.

Counterfactual evaluation. Following Zheng et al. (2023), we also apply counterfactual evaluation (Hooker et al., 2019). We assess the relative change in model property, $\Delta\mathcal{F} = \frac{\mathcal{F}(\theta_k^*) - \mathcal{F}(\theta^*)}{\mathcal{F}(\theta^*)}$, by comparing the models trained before and after excluding (or retaining only) the top k most influential contributors identified by each attribution method. Counterfactual evaluation requires retraining models on different subsets for each method, so only baseline methods with the best LDS in each category are chosen for computational feasibility.

4.5 EXPERIMENT RESULTS

SHAPLEY ATTRIBUTION OUTPERFORMS BASELINE METHODS IN CONTRIBUTOR ATTRIBUTION

In Table 1, we present the LDS results for baseline methods and our approach. Interestingly, similarity-based methods such as raw pixel similarity, CLIP similarity, and gradient similarity occasionally

⁵<https://github.com/LAION-AI/aesthetic-predictor>

⁶TracIn (Pruthi et al., 2020) is not considered since intermediate checkpoints may not be available in practice.

outperform TRAK-based methods. We observe that TRAK-based methods sometimes yield poor or even negative correlations. Among TRAK-based approaches, attribution using noisy latents during generation (i.e., Journey-TRAK) can result in a negative LDS for model properties such as the Inception Score and aesthetic score. Our findings indicate that simply aggregating individual attributions derived from diffusion loss or its alternative functions is insufficient for accurately determining contributor attribution of global properties. Such an approach can perform worse than simple heuristics based on model properties (e.g., the average aesthetic score).

Table 1: LDS (%) results with $\alpha = 0.5$. Means and 95% confidence intervals across three random initializations are reported.

Method	CIFAR-20	CelebA-HQ	ArtBench (Post-Impressionism)
Pixel similarity (average)	-11.81 \pm 4.56	-8.91 \pm 0.93	11.24 \pm 0.63
Pixel similarity (max)	-31.80 \pm 2.90	21.70 \pm 2.05	14.61 \pm 2.72
Embedding dist. (average)	-	13.83 \pm 1.12	-
Embedding dist. (max)	-	7.32 \pm 3.16	-
CLIP similarity (average)	5.79 \pm 3.67	-32.23 \pm 0.87	-6.96 \pm 4.08
CLIP similarity (max)	11.31 \pm 0.37	-0.93 \pm 3.83	-1.75 \pm 4.07
Gradient similarity (average)	5.79 \pm 3.67	-18.32 \pm 0.65	0.25 \pm 1.18
Gradient similarity (max)	-0.89 \pm 3.17	-12.90 \pm 1.60	10.48 \pm 3.11
Aesthetic score (average)	-	-	24.85 \pm 2.30
Aesthetic score (max)	-	-	21.36 \pm 3.70
Relative IF	5.23 \pm 5.50	-1.07 \pm 0.68	-5.02 \pm 1.77
Renormalized IF	11.39 \pm 6.79	10.17 \pm 0.57	-11.41 \pm 0.93
TRAK	7.94 \pm 5.67	3.22 \pm 0.75	-8.18 \pm 1.30
Journey-TRAK	-42.92 \pm 2.15	-2.88 \pm 4.02	-11.41 \pm 4.22
D-TRAK	10.90 \pm 1.21	-27.23 \pm 2.80	11.30 \pm 3.47
Leave-one-out (LOO)	30.66 \pm 6.11	-1.22 \pm 6.34	3.74 \pm 8.00
Sparsified-FT Shapley (Ours)	61.48 \pm 2.27	26.34 \pm 3.42	61.44 \pm 2.04

In contrast, our approach, sparsified-fine-tuning (sparsified-FT) Shapley, computes contributor attribution using the Shapley value, achieving the highest LDS results of 61.48%, 26.34%, and 61.44% for CIFAR-20, CelebA-HQ, and ArtBench (Post-Impressionism), respectively. While leave-one-out (LOO) achieves 30.66% LDS on CIFAR-20, its performance declines as the number of contributors increase, e.g., CelebA-HQ and ArtBench (Post-Impressionism). This shows that attribution based on the marginal contribution of Shapley subsets with respect to \mathcal{F} provides the most accurate importance score. Despite achieving the best results for CelebA-HQ compared to the baseline methods, we observe that the LDS performance of sparsified-FT Shapley, 26.32%, is relatively low compared to those of CIFAR-20 and ArtBench. We also perform evaluation across varying datamodel subset sizes ($\alpha = 0.25, 0.5, 0.75$), and our approach consistently outperforms others (Appendix F).

ENHANCING RETRAINING AND INFERENCE EFFICIENCY THROUGH SPARSIFIED FINE-TUNING

As described in Section 3.2, computing $\mathcal{F}(\theta_{S_j}^*)$ is the primary computational bottleneck. Our sparsified fine-tuning approach significantly reduces the runtime required to obtain $\theta_{S_j}^*$ compared to retraining and fine-tuning without sparsification. On average, retraining and inference with sparsified fine-tuning for a Shapley subset take 18.3 minutes for CIFAR-20, 22.9 minutes for CelebA-HQ, and 10.5 minutes for ArtBench (Post-Impressionism), making it 5.3, 10.4, and 18.6 times faster than retraining, respectively (Table 2). By enabling faster computation and obtaining more models retrained on different subsets, sparsified FT yields the best LDS results under the same computational budgets (Figure 2). This demonstrates that sparsified-FT Shapley is both more computationally feasible and accurate with limited computational resources. To the best of our knowledge, we are the first to overcome the computational bottleneck and enable contributor attribution using Shapley values for diffusion models.

432
433
434
435
436
437
438
439
440
441
442
443
444
445
446
447
448
449
450
451
452
453
454
455
456
457
458
459
460
461
462
463
464
465
466
467
468
469
470
471
472
473
474
475
476
477
478
479
480
481
482
483
484
485

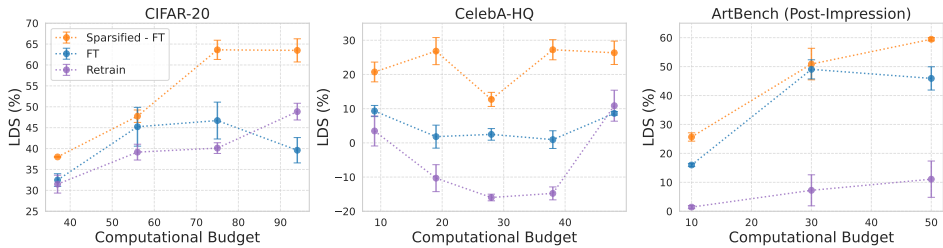


Figure 2: Comparison of LDS (%) with $\alpha = 0.5$ among Shapley values estimated with sparsified fine-tuning (FT), fine-tuning (FT), and retraining under the same computational budgets (1 unit = runtime to retrain and run inference on a full model). Specific runtimes are shown in Table 2.

IMPACT OF CONTRIBUTORS ON MODEL PROPERTY

Here we present the results of our counterfactual evaluation, analyzing changes in model behavior after either removing the top contributors or including only the top contributors identified by each method. In CIFAR-20, our approach shows a change of -23.23%, compared to -14.95% for CLIP similarity and -17.30% for LOO, as shown in Figure 3 (top). For CelebA-HQ, the changes are -7.83% for our method, -6.64% for pixel similarity, and 0.21% for renormalized IF. For ArtBench (Post-Impressionism), the changes are 0.58%, -0.05%, -1.27%, and -1.86% for D-TRAK, maximum pixel similarity, average aesthetic score, and sparsified-FT Shapley, respectively.

Conversely, when retaining the top 60% of contributors, model properties improve. In the CIFAR-20 dataset, our method leads to a 16.98% positive change in model properties, compared to -9.45% for CLIP similarity and 9.51% for LOO. For CelebA-HQ, the model behavior change was 20.0% for our method, 8.89% for pixel similarity, and 6.02% for renormalized IF (bottom of Figure 3). These findings, along with the results in Section 4.5, demonstrate that our approach effectively identifies the top contributors and provides accurate attribution.

WHO ARE THE TOP CONTRIBUTORS?

We analyze the top contributors identified by sparsified-FT Shapley in CIFAR-20, including contributors to classes such as motorcycles, buses, and lawnmowers (Figure 4). High-quality labeling by these contributors ensures that the training images contain clear and meaningful objects, which should result in low entropy (i.e., high confidence) of a classifier (i.e., Inception v3) (Barratt & Sharma, 2018). We therefore compute the entropy of each image and find that the top 20% classes have a lower average entropy of 5.18, compared to 6.03 for the remaining classes (Figure 16). For CelebA-HQ, the most important celebrities ranked by sparsified-FT Shapley encompass a diverse range of demographics and tend to belong to non-majority demographic clusters (Figure 16). Excluding images corresponding to these celebrities can have a negative impact on the diversity score. For ArtBench, we observe that images from the top contributors are more vivid and exhibit more vibrant colors, as shown in Figure 4.

5 DISCUSSION

In this work, we introduce the problem of attributing global model properties to data contributors in the context of diffusion models. To address this problem, we develop an efficient framework that estimates the Shapley values for data contributors by leveraging model pruning and fine-tuning. This approach speeds up retraining and improves inference runtime, while ensuring accurate attribution. Our framework can have wide-ranging implications, such as creating incentives for data contributors, rewarding data labelers in a way that satisfies game-theoretic fairness, assessing labeling quality, and improving model performance and fairness. Empirical results across multiple datasets and global model properties show that our framework outperforms existing attribution approaches based on the diffusion loss, such as TRAK (Park et al., 2023) and its variant D-TRAK (Zheng et al., 2023), in crediting data contributors. There are several promising directions for future research. First, beyond fine-tuning, recent unlearning methods designed for diffusion models (Gandikota et al., 2023; Heng

486
487
488
489
490
491
492
493
494
495
496
497
498
499
500
501
502
503
504
505
506
507
508
509
510
511
512
513
514
515
516
517
518
519
520
521
522
523
524
525
526
527
528
529
530
531
532
533
534
535
536
537
538
539

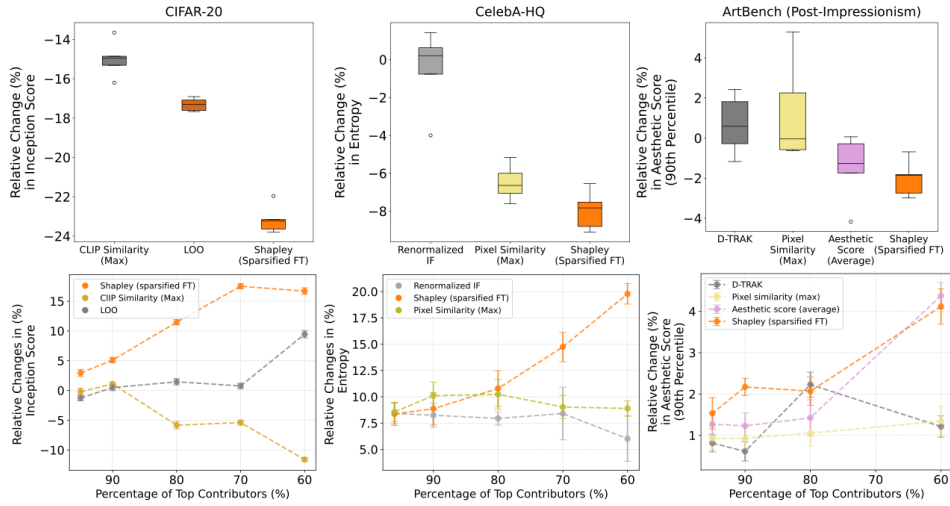


Figure 3: Relative percentage changes in global properties, comparing the original fully trained models to models retrained after removing the top 40% contributors (top) and including only the top contributors (bottom), as identified by various attribution methods.



Figure 4: Top contributors and their corresponding training images for each dataset (top). Pairs of generated images above and below the 90th percentile of aesthetic score from Stable Diffusion models LoRA-finetuned under three conditions: excluding the data from the top 40% of artists, using the data from all the artists, and including only the data from the top 60% of artists (bottom).

& Soh, 2023) could be explored in combination with various pruning strategies (Ding et al., 2019; Fang et al., 2024; Liu et al., 2021). Second, it can be useful to allocate contributor-level importance to datum-level importance for the data provided by each contributor, providing attribution at two levels of granularity. The Owen value, which modifies the Shapley value, is well suited for this scenario (Owen, 1977). Beyond diffusion models, our proposed framework can also be extended to models that are expensive to retrain, such as large language models (LLMs), whenever appropriate pruning and unlearning approaches are available. Finally, our approach and existing attribution methods for diffusion models assume access to training data and model parameters, which are not necessarily available for deployed models. For text-to-image models, membership inference and in-context learning may be useful in addressing this challenge (Hu & Pang, 2023; Wang et al., 2023b).

6 ETHICS STATEMENT

As diffusion models become increasingly deployed in real-world applications, there is a notable lack of clear guidelines for crediting data contributors. This work focuses on the fair attribution of data contributors for diffusion models, which is a crucial step towards creating incentives for sharing quality data and implementing policies for equitable compensation. By efficiently estimating Shapley values, our approach can promote fairness in recognizing the importance of data contributors. Importantly, our approach is motivated by positive attribution, such as incentivizing quality labeling and improving the demographic diversity of generated images. However, we also recognize that our approach could potentially be used to remove data from certain data contributors. We view this as an opportunity to ensure higher data quality and transparency in model development, particularly when addressing harmful or irrelevant contributions. Ensuring data contributors are fairly compensated and informed is critical to avoid exploitation. Our use cases, such as demographic diversity for CelebA-HQ, highlight the need for transparency in data usage and advocate for diverse and representative datasets. At the same time, we acknowledge that considerations related to data privacy, consent, and the potential amplification of biases, especially in socially sensitive applications, may not be easily quantified as model properties.

REFERENCES

- Shane Barratt and Rishi Sharma. A note on the inception score. *arXiv preprint arXiv:1801.01973*, 2018.
- Elnaz Barshan, Marc-Etienne Brunet, and Gintare Karolina Dziugaite. Relatif: Identifying explanatory training samples via relative influence. In *International Conference on Artificial Intelligence and Statistics*, pp. 1899–1909. PMLR, 2020.
- Guillaume Charpiat, Nicolas Girard, Loris Felardos, and Yuliya Tarabalka. Input similarity from the neural network perspective. *Advances in Neural Information Processing Systems*, 32, 2019.
- Ian Covert and Su-In Lee. Improving KernelSHAP: Practical Shapley value estimation using linear regression. In *International Conference on Artificial Intelligence and Statistics*, pp. 3457–3465. PMLR, 2021.
- Ian Covert, Scott Lundberg, and Su-In Lee. Feature removal is a unifying principle for model explanation methods. *arXiv preprint arXiv:2011.03623*, 2020.
- Zheng Dai and David K Gifford. Training data attribution for diffusion models. *arXiv preprint arXiv:2306.02174*, 2023.
- Tim Dettmers, Mike Lewis, Sam Shleifer, and Luke Zettlemoyer. 8-bit optimizers via block-wise quantization. In *The Tenth International Conference on Learning Representations, ICLR 2022, Virtual Event, April 25-29, 2022*. OpenReview.net, 2022. URL <https://openreview.net/forum?id=shpkpVXzo3h>.
- Prafulla Dhariwal and Alexander Nichol. Diffusion models beat gans on image synthesis. *Advances in neural information processing systems*, 34:8780–8794, 2021.
- Xiaohan Ding, Guiguang Ding, Yuchen Guo, and Jungong Han. Centripetal sgd for pruning very deep convolutional networks with complicated structure. In *Proceedings of the IEEE/CVF conference on computer vision and pattern recognition*, pp. 4943–4953, 2019.
- Gongfan Fang, Xinyin Ma, and Xinchao Wang. Structural pruning for diffusion models. *arXiv preprint arXiv:2305.10924*, 2023.
- Gongfan Fang, Xinyin Ma, and Xinchao Wang. Structural pruning for diffusion models. *Advances in neural information processing systems*, 36, 2024.
- Jonathan Frankle and Michael Carbin. The lottery ticket hypothesis: Finding sparse, trainable neural networks. *arXiv preprint arXiv:1803.03635*, 2018.
- Rohit Gandikota, Joanna Materzynska, Jaden Fiotto-Kaufman, and David Bau. Erasing concepts from diffusion models. *arXiv preprint arXiv:2303.07345*, 2023.

- 594 Kristian Georgiev, Joshua Vendrow, Hadi Salman, Sung Min Park, and Aleksander Madry. The
595 journey, not the destination: How data guides diffusion models. *arXiv preprint arXiv:2312.06205*,
596 2023.
- 597 Kristian Georgiev, Roy Rinberg, Sung Min Park, Shivam Garg, Andrew Ilyas, Aleksander Madry,
598 and Seth Neel. Attribute-to-delete: Machine unlearning via datamodel matching. *arXiv preprint*
599 *arXiv:2410.23232*, 2024.
- 600 Amirata Ghorbani and James Zou. Data shapley: Equitable valuation of data for machine learning.
601 In *International conference on machine learning*, pp. 2242–2251. PMLR, 2019.
- 602 Aditya Golatkar, Alessandro Achille, and Stefano Soatto. Eternal sunshine of the spotless net:
603 Selective forgetting in deep networks. In *Proceedings of the IEEE/CVF Conference on Computer*
604 *Vision and Pattern Recognition*, pp. 9304–9312, 2020.
- 605 Ian J Goodfellow, Jonathon Shlens, and Christian Szegedy. Explaining and harnessing adversarial
606 examples. *arXiv preprint arXiv:1412.6572*, 2014.
- 607 Laura Graves, Vineel Nagisetty, and Vijay Ganesh. Amnesiac machine learning. In *Proceedings of*
608 *the AAAI Conference on Artificial Intelligence*, volume 35, pp. 11516–11524, 2021.
- 609 Zayd Hammoudeh and Daniel Lowd. Identifying a training-set attack’s target using renormalized
610 influence estimation. In *Proceedings of the 2022 ACM SIGSAC Conference on Computer and*
611 *Communications Security*, pp. 1367–1381, 2022.
- 612 Song Han, Jeff Pool, John Tran, and William Dally. Learning both weights and connections for
613 efficient neural network. *Advances in neural information processing systems*, 28, 2015.
- 614 Alvin Heng and Harold Soh. Selective amnesia: A continual learning approach to forgetting in deep
615 generative models. *arXiv preprint arXiv:2305.10120*, 2023.
- 616 Martin Heusel, Hubert Ramsauer, Thomas Unterthiner, Bernhard Nessler, and Sepp Hochreiter. Gans
617 trained by a two time-scale update rule converge to a local nash equilibrium. *Advances in neural*
618 *information processing systems*, 30, 2017.
- 619 Jonathan Ho, Ajay Jain, and Pieter Abbeel. Denoising diffusion probabilistic models. *Advances in*
620 *neural information processing systems*, 33:6840–6851, 2020.
- 621 Sara Hooker, Dumitru Erhan, Pieter-Jan Kindermans, and Been Kim. A benchmark for interpretability
622 methods in deep neural networks. *Advances in neural information processing systems*, 32, 2019.
- 623 Edward J Hu, Yelong Shen, Phillip Wallis, Zeyuan Allen-Zhu, Yuanzhi Li, Shean Wang, Lu Wang,
624 and Weizhu Chen. Lora: Low-rank adaptation of large language models. *arXiv preprint*
625 *arXiv:2106.09685*, 2021.
- 626 Hailong Hu and Jun Pang. Membership inference of diffusion models. *arXiv preprint*
627 *arXiv:2301.09956*, 2023.
- 628 Andrew Ilyas, Sung Min Park, Logan Engstrom, Guillaume Leclerc, and Aleksander Madry. Data-
629 models: Predicting predictions from training data. *arXiv preprint arXiv:2202.00622*, 2022.
- 630 Zachary Izzo, Mary Anne Smart, Kamalika Chaudhuri, and James Zou. Approximate data deletion
631 from machine learning models. In *International Conference on Artificial Intelligence and Statistics*,
632 pp. 2008–2016. PMLR, 2021.
- 633 Ward Jh Jr. Hierarchical grouping to optimize an objective function. *J. Am. Stat. Assoc.*, 58:
634 236–244, 1963.
- 635 Jinghan Jia, Jiancheng Liu, Parikshit Ram, Yuguang Yao, Gaowen Liu, Yang Liu, Pranay Sharma,
636 and Sijia Liu. Model sparsity can simplify machine unlearning. In *Annual Conference on Neural*
637 *Information Processing Systems*, 2023.
- 638 Harry H Jiang, Lauren Brown, Jessica Cheng, Mehtab Khan, Abhishek Gupta, Deja Workman, Alex
639 Hanna, Johnathan Flowers, and Timnit Gebru. Ai art and its impact on artists. In *Proceedings of*
640 *the 2023 AAAI/ACM Conference on AI, Ethics, and Society*, pp. 363–374, 2023.

- 648 Tero Karras, Timo Aila, Samuli Laine, and Jaakko Lehtinen. Progressive growing of gans for
649 improved quality, stability, and variation. In *6th International Conference on Learning Representations, ICLR 2018, Vancouver, BC, Canada, April 30 - May 3, 2018, Conference Track Proceedings*.
650 OpenReview.net, 2018. URL <https://openreview.net/forum?id=Hk99zCeAb>.
651
- 652 Tero Karras, Miika Aittala, Timo Aila, and Samuli Laine. Elucidating the design space of diffusion-
653 based generative models. *Advances in Neural Information Processing Systems*, 35:26565–26577,
654 2022.
655
- 656 Pang Wei Koh and Percy Liang. Understanding black-box predictions via influence functions. In
657 *International conference on machine learning*, pp. 1885–1894. PMLR, 2017.
658
- 659 Pang Wei W Koh, Kai-Siang Ang, Hubert Teo, and Percy S Liang. On the accuracy of influence
660 functions for measuring group effects. *Advances in neural information processing systems*, 32,
661 2019.
- 662 Alex Krizhevsky, Geoffrey Hinton, et al. Learning multiple layers of features from tiny images. 2009.
663
- 664 Yongchan Kwon and James Zou. Beta shapley: a unified and noise-reduced data valuation framework
665 for machine learning. *arXiv preprint arXiv:2110.14049*, 2021.
666
- 667 Junnan Li, Dongxu Li, Caiming Xiong, and Steven Hoi. Blip: Bootstrapping language-image pre-
668 training for unified vision-language understanding and generation. In *International conference on*
669 *machine learning*, pp. 12888–12900. PMLR, 2022.
- 670 Peiyuan Liao, Xiuyu Li, Xihui Liu, and Kurt Keutzer. The artbench dataset: Benchmarking generative
671 models with artworks. *arXiv preprint arXiv:2206.11404*, 2022.
672
- 673 Liyang Liu, Shilong Zhang, Zhanghui Kuang, Aojun Zhou, Jing-Hao Xue, Xinjiang Wang, Yimin
674 Chen, Wenming Yang, Qingmin Liao, and Wayne Zhang. Group fisher pruning for practical
675 network compression. In *International Conference on Machine Learning*, pp. 7021–7032. PMLR,
676 2021.
- 677 Ilya Loshchilov and Frank Hutter. Decoupled weight decay regularization. *arXiv preprint*
678 *arXiv:1711.05101*, 2017.
679
- 680 Alexandra Sasha Luccioni, Christopher Akiki, Margaret Mitchell, and Yacine Jernite. Stable bias:
681 Analyzing societal representations in diffusion models. *arXiv preprint arXiv:2303.11408*, 2023.
682
- 683 Scott M Lundberg and Su-In Lee. A unified approach to interpreting model predictions. In *Advances*
684 *in Neural Information Processing Systems*, pp. 4765–4774, 2017.
- 685 Guillermo Owen. Values of games with a priori unions. In *Mathematical economics and game*
686 *theory: Essays in honor of Oskar Morgenstern*, pp. 76–88. Springer, 1977.
687
- 688 Sung Min Park, Kristian Georgiev, Andrew Ilyas, Guillaume Leclerc, and Aleksander Madry. Trak:
689 Attributing model behavior at scale. *arXiv preprint arXiv:2303.14186*, 2023.
- 690 Garima Pruthi, Frederick Liu, Satyen Kale, and Mukund Sundararajan. Estimating training data
691 influence by tracing gradient descent. *Advances in Neural Information Processing Systems*, 33:
692 19920–19930, 2020.
693
- 694 Alec Radford, Jong Wook Kim, Chris Hallacy, Aditya Ramesh, Gabriel Goh, Sandhini Agarwal,
695 Girish Sastry, Amanda Askell, Pamela Mishkin, Jack Clark, et al. Learning transferable visual
696 models from natural language supervision. In *International conference on machine learning*, pp.
697 8748–8763. PMLR, 2021.
- 698 Aditya Ramesh, Prafulla Dhariwal, Alex Nichol, Casey Chu, and Mark Chen. Hierarchical text-
699 conditional image generation with clip latents. *arXiv preprint arXiv:2204.06125*, 1(2):3, 2022.
700
- 701 Ali Razavi, Aaron Van den Oord, and Oriol Vinyals. Generating diverse high-fidelity images with
vq-vae-2. *Advances in neural information processing systems*, 32, 2019.

- 702 Robin Rombach, Andreas Blattmann, Dominik Lorenz, Patrick Esser, and Björn Ommer. High-
703 resolution image synthesis with latent diffusion models. In *Proceedings of the IEEE/CVF conference on computer vision and pattern recognition*, pp. 10684–10695, 2022.
704
705 Nataniel Ruiz, Yuanzhen Li, Varun Jampani, Yael Pritch, Michael Rubinstein, and Kfir Aberman.
706 Dreambooth: Fine tuning text-to-image diffusion models for subject-driven generation. In *Proceedings of the IEEE/CVF Conference on Computer Vision and Pattern Recognition*, pp. 22500–22510,
707 2023.
708
709 Tim Salimans, Ian Goodfellow, Wojciech Zaremba, Vicki Cheung, Alec Radford, and Xi Chen.
710 Improved techniques for training gans. *Advances in neural information processing systems*, 29,
711 2016.
712
713 Christoph Schuhmann, Romain Beaumont, Richard Vencu, Cade Gordon, Ross Wightman, Mehdi
714 Cherti, Theo Coombes, Aarush Katta, Clayton Mullis, Mitchell Wortsman, et al. Laion-5b: An
715 open large-scale dataset for training next generation image-text models. *Advances in Neural
716 Information Processing Systems*, 35:25278–25294, 2022.
717
718 Lloyd S Shapley. A value for n-person games. *Contributions to the Theory of Games*, 2(28):307–317,
719 1953.
720
721 Jiaming Song, Chenlin Meng, and Stefano Ermon. Denoising diffusion implicit models. *arXiv
722 preprint arXiv:2010.02502*, 2020a.
723
724 Yang Song, Jascha Sohl-Dickstein, Diederik P Kingma, Abhishek Kumar, Stefano Ermon, and Ben
725 Poole. Score-based generative modeling through stochastic differential equations. *arXiv preprint
726 arXiv:2011.13456*, 2020b.
727
728 Charles Spearman. The proof and measurement of association between two things. 1961.
729
730 Erik Štrumbelj and Igor Kononenko. An efficient explanation of individual classifications using game
731 theory. *Journal of Machine Learning Research*, 11:1–18, 2010.
732
733 Jiachen T Wang and Ruoxi Jia. Data banzhaf: A robust data valuation framework for machine
734 learning. In *International Conference on Artificial Intelligence and Statistics*, pp. 6388–6421.
735 PMLR, 2023.
736
737 Sheng-Yu Wang, Alexei A Efros, Jun-Yan Zhu, and Richard Zhang. Evaluating data attribution for
738 text-to-image models. *arXiv preprint arXiv:2306.09345*, 2023a.
739
740 Zhendong Wang, Yifan Jiang, Yadong Lu, Pengcheng He, Weizhu Chen, Zhangyang Wang, Mingyuan
741 Zhou, et al. In-context learning unlocked for diffusion models. *Advances in Neural Information
742 Processing Systems*, 36:8542–8562, 2023b.
743
744 David Gray Widder, Sarah West, and Meredith Whittaker. Open (for business): Big tech, concentrated
745 power, and the political economy of open ai. *Concentrated Power, and the Political Economy of
746 Open AI (August 17, 2023)*, 2023.
747
748 Matteo Wong. America already has an ai underclass. *The Atlantic*, 2023.
749
750 Xiaosen Zheng, Tianyu Pang, Chao Du, Jing Jiang, and Min Lin. Intriguing properties of data
751 attribution on diffusion models. *arXiv preprint arXiv:2311.00500*, 2023.
752
753
754
755

APPENDIX

A PROOFS

Before proving Proposition 1, we first provide the following lemma.

Lemma 1. *Suppose an objective function $\ell : \mathbb{R}^d \mapsto \mathbb{R}$ is convex and differentiable, and that its gradient is Lipschitz-continuous with some constant $L > 0$, i.e.*

$$\|\nabla\ell(\theta_1) - \nabla\ell(\theta_2)\|_2 \leq L\|\theta_1 - \theta_2\|_2$$

for any $\theta_1, \theta_2 \in \mathbb{R}^d$. Then running gradient descent for k steps with learning rate $\alpha \leq 1/L$ satisfies

$$\ell(\theta^{(k)}) - \ell(\theta^*) \leq \frac{\|\theta^{(0)} - \theta^*\|_2^2}{2k\alpha},$$

where $\theta^{(k)}$ is the model parameter after the k th step, θ^* is the optimum, and $\theta^{(0)}$ is the initial parameter.

Proof. We provide the proof for this well-known result for completeness. The assumption that $\nabla\ell(\theta)$ is L -Lipschitz continuous implies that $\nabla^2\ell(\theta) \preceq LI$, so we can perform a quadratic expansion of ℓ around $\ell(\theta)$ to obtain the following inequality:

$$\ell(\theta^{(i)}) \leq \ell(\theta) + \nabla\ell(\theta)^\top(\theta^{(i)} - \theta) + \frac{1}{2}L\|\theta^{(i)} - \theta\|_2^2, \quad (11)$$

for any $\theta, \theta^{(i)} \in \mathbb{R}^d$. With the gradient descent update $\theta^{(i)} = \theta^{(i-1)} - \alpha\nabla\ell(\theta^{(i-1)})$ and setting $\theta = \theta^{(i-1)}$ in Equation (11), we obtain

$$\ell(\theta^{(i)}) \leq \ell(\theta^{(i-1)}) + \nabla\ell(\theta^{(i-1)})^\top\alpha\nabla\ell(\theta^{(i-1)}) + \frac{1}{2}L\|\alpha\nabla\ell(\theta^{(i-1)})\|_2^2 \quad (12)$$

$$= \ell(\theta^{(i-1)}) - \alpha\|\nabla\ell(\theta^{(i-1)})\|_2^2 + \frac{1}{2}\alpha^2L\|\nabla\ell(\theta^{(i-1)})\|_2^2 \quad (13)$$

$$= \ell(\theta^{(i-1)}) - \left(1 - \frac{1}{2}\alpha L\right)\alpha\|\nabla\ell(\theta^{(i-1)})\|_2^2. \quad (14)$$

Using $\alpha \leq 1/L$, we have

$$1 - \frac{1}{2}\alpha L \geq 1 - \frac{1}{2} \cdot \frac{1}{L} \cdot L = \frac{1}{2}. \quad (15)$$

Hence

$$\ell(\theta^{(i)}) \leq \ell(\theta^{(i-1)}) - \frac{1}{2}\alpha\|\nabla\ell(\theta^{(i-1)})\|_2^2, \quad (16)$$

which implies that the objective is decreasing until the optimal value is reached, because $\|\nabla\ell(\theta^{(i-1)})\|_2^2$ is positive unless $\nabla\ell(\theta^{(i-1)}) = 0$.

Now since ℓ is convex, we have

$$\ell(\theta^{(i-1)}) + \nabla\ell(\theta^{(i-1)})^\top(\theta^* - \theta^{(i-1)}) \leq \ell(\theta^*), \quad (17)$$

and

$$\ell(\theta^{(i-1)}) \leq \ell(\theta^*) + \nabla\ell(\theta^{(i-1)})^\top(\theta^{(i-1)} - \theta^*) \quad (18)$$

after rearrangement. Plugging this inequality into Equation (16), we have

$$\ell(\theta^{(i)}) \leq \ell(\theta^*) + \nabla\ell(\theta^{(i-1)})^\top(\theta^{(i-1)} - \theta^*) - \frac{1}{2}\alpha\|\nabla\ell(\theta^{(i-1)})\|_2^2, \quad (19)$$

which implies that

$$\ell(\theta^{(i)}) - \ell(\theta^*) \quad (20)$$

$$\leq \nabla\ell(\theta^{(i-1)})^\top(\theta^{(i-1)} - \theta^*) - \frac{1}{2}\alpha\|\nabla\ell(\theta^{(i-1)})\|_2^2 \quad (21)$$

$$= \frac{1}{2\alpha} \left(2\alpha\nabla\ell(\theta^{(i-1)})^\top(\theta^{(i-1)} - \theta^*) - \alpha^2\|\nabla\ell(\theta^{(i-1)})\|_2^2 \right) \quad (22)$$

$$= \frac{1}{2\alpha} \left(2\alpha\nabla\ell(\theta^{(i-1)})^\top(\theta^{(i-1)} - \theta^*) - \alpha^2\|\nabla\ell(\theta^{(i-1)})\|_2^2 - \|\theta^{(i-1)} - \theta^*\|_2^2 + \|\theta^{(i-1)} - \theta^*\|_2^2 \right) \quad (23)$$

$$= \frac{1}{2\alpha} \left(\|\theta^{(i-1)} - \theta^*\|_2^2 - \|\theta^{(i-1)} - \alpha\nabla\ell(\theta^{(i-1)}) - \theta^*\|_2^2 \right). \quad (24)$$

Plugging in the gradient descent update rule into this inequality, we get

$$\ell(\theta^{(i)}) - \ell(\theta^*) \leq \frac{1}{2\alpha} \left(\|\theta^{(i-1)} - \theta^*\|_2^2 - \|\theta^{(i)} - \theta^*\|_2^2 \right). \quad (25)$$

Summing over k steps, we have

$$\sum_{i=1}^k \ell(\theta^{(i)}) - \ell(\theta^*) \leq \sum_{i=1}^k \frac{1}{2\alpha} \left(\|\theta^{(i-1)} - \theta^*\|_2^2 - \|\theta^{(i)} - \theta^*\|_2^2 \right) \quad (26)$$

$$= \frac{1}{2\alpha} \left(\|\theta^{(0)} - \theta^*\|_2^2 - \|\theta^{(k)} - \theta^*\|_2^2 \right) \quad (27)$$

$$\leq \frac{1}{2\alpha} \|\theta^{(0)} - \theta^*\|_2^2 \quad (28)$$

, where the telescoping sum results in the equality. Finally, the term in the summation on the LHS is decreasing because of Equation (16), hence

$$\ell(\theta^{(k)}) - \ell(\theta^*) \leq \frac{1}{k} \sum_{i=1}^k \ell(\theta^{(i)}) - \ell(\theta^*) \leq \frac{\|\theta^{(0)} - \theta^*\|_2^2}{2k\alpha}. \quad (29)$$

□

We then proceed to prove Proposition 1.

Proof of Proposition 1. By the triangle inequality, we have

$$\mathbb{E}[|\mathcal{F}(\tilde{\theta}_{S,k}^{\text{ft}}) - \mathcal{F}(\theta_S^*)|] \leq \mathbb{E}[|\mathcal{F}(\tilde{\theta}_{S,k}^{\text{ft}}) - \mathcal{F}(\tilde{\theta}_S^*)|] + \mathbb{E}[|\mathcal{F}(\tilde{\theta}_S^*) - \mathcal{F}(\theta_S^*)|] \quad (30)$$

$$\leq \mathbb{E}[|\mathcal{F}(\tilde{\theta}_{S,k}^{\text{ft}}) - \mathcal{F}(\tilde{\theta}_S^*)|] + B, \quad (31)$$

where the second inequality comes from the assumption that $\mathbb{E}[|\mathcal{F}(\tilde{\theta}_S^*) - \mathcal{F}(\theta_S^*)|] \leq B$.

Note that $\tilde{\theta}_{S,k}^{\text{ft}}$ and $\tilde{\theta}_S^*$ are in \mathbb{R}^d , with zeros for the pruned weights. Hence the assumptions on ℓ hold for $\tilde{\theta}_{S,k}^{\text{ft}}, \tilde{\theta}_S^*$. Applying Lemma 1, we have

$$\ell(\tilde{\theta}_{S,k}^{\text{ft}}) - \ell(\tilde{\theta}_S^*) \leq \frac{\|\tilde{\theta}_S^* - \tilde{\theta}_{S,k}^{\text{ft}}\|_2^2}{2k\alpha}, \quad (32)$$

where we recall that $\tilde{\theta}_S^*$ denotes the pruned model before fine-tuning. Taking $k \rightarrow \infty$, we obtain $\ell(\tilde{\theta}_{S,k}^{\text{ft}}) - \ell(\tilde{\theta}_S^*) = 0$, and it follows that $\tilde{\theta}_{S,k}^{\text{ft}} = \tilde{\theta}_S^*$ because ℓ is convex. Therefore, as $k \rightarrow \infty$, we have

$$\mathbb{E}[|\mathcal{F}(\tilde{\theta}_{S,k}^{\text{ft}}) - \mathcal{F}(\theta_S^*)|] \leq \mathbb{E}[|\mathcal{F}(\tilde{\theta}_{S,k}^{\text{ft}}) - \mathcal{F}(\tilde{\theta}_S^*)|] + B \quad (33)$$

$$= \mathbb{E}[|\mathcal{F}(\tilde{\theta}_S^*) - \mathcal{F}(\theta_S^*)|] + B \quad (34)$$

$$= B \quad (35)$$

□

Before proving Proposition 2, we provide the following lemma.

Lemma 2. *The exact Shapley values $\beta \in \mathbb{R}^n$ for the data contributors evaluated with $\{\mathcal{F}(\theta_S)\}_{S \in 2^{\mathcal{D}}}$ can be represented as $\beta = Av$, where $A \in \mathbb{R}^{n \times 2^n}$ is a matrix with rows indexed by the data contributors and columns indexed by all possible contributor subsets, and $v \in \mathbb{R}^{2^n}$ is a vector indexed by all possible contributor subsets. Specifically,*

$$A[i, S] = \begin{cases} \frac{1}{n} \binom{n-1}{|S|-1}^{-1}, & \text{if } C_i \in S \\ -\frac{1}{n} \binom{n-1}{|S|}^{-1}, & \text{otherwise} \end{cases} \quad (36)$$

and $v[S] = \mathcal{F}(\theta_S)$.

864 *Proof.* For each data contributor i , we have

$$865 \beta_i = \sum_{S \in 2^{\mathcal{D}}} A[i, S] \cdot v[S] \quad (37)$$

$$866 = \sum_{S: C_i \in S} \frac{1}{n} \binom{n-1}{|S|-1}^{-1} \mathcal{F}(\theta_S) - \sum_{S': C_i \notin S'} \frac{1}{n} \binom{n-1}{|S'|}^{-1} \mathcal{F}(\theta_{S'}) \quad (38)$$

$$867 = \sum_{S' \subseteq \mathcal{D} \setminus C_i} \frac{1}{n} \binom{n-1}{|S'|}^{-1} \mathcal{F}(\theta_{S' \cup C_i}) - \sum_{S' \subseteq \mathcal{D} \setminus C_i} \frac{1}{n} \binom{n-1}{|S'|}^{-1} \mathcal{F}(\theta_{S'}) \quad (39)$$

$$870 = \frac{1}{n} \sum_{S' \subseteq \mathcal{D} \setminus C_i} \binom{n-1}{|S'|}^{-1} (\mathcal{F}(\theta_{S' \cup C_i}) - \mathcal{F}(\theta_{S'})), \quad (40)$$

871 which is the Shapley value for contributor i . The third equality follows from the change of variable
872 $S' = S \setminus C_i$ such that $|S'| = |S| - 1$. \square

873 Finally, we prove Proposition 2 as follows.

874 *Proof of Proposition 2.* Based on Lemma 2, $\tilde{\beta}_k^{\text{ft}} = A\tilde{v}_k^{\text{ft}}$, and $\beta^* = Av^*$, where $\tilde{v}_k^{\text{ft}}[S] = \mathcal{F}(\tilde{\theta}_{S,k}^{\text{ft}})$ and
875 $v^*[S] = \mathcal{F}(\theta_S^*)$ for all $S \in 2^{\mathcal{D}}$. Hence we have

$$876 \mathbb{E}[\|\tilde{\beta}_k^{\text{ft}} - \beta^*\|_2] = \mathbb{E}[\|A\tilde{v}_k^{\text{ft}} - Av^*\|_2] \quad (41)$$

$$877 = \mathbb{E}\left[\sqrt{\sum_{i=1}^n (A[i]^\top (\tilde{v}_k^{\text{ft}} - v^*))^2}\right] \quad (42)$$

$$878 \leq \mathbb{E}\left[\sqrt{\sum_{i=1}^n \|A[i]\|_1^2 \cdot \|\tilde{v}_k^{\text{ft}} - v^*\|_\infty^2}\right] \quad (43)$$

$$879 = \mathbb{E}\|\tilde{v}_k^{\text{ft}} - v^*\|_\infty \cdot \sqrt{\sum_{i=1}^n \|A[i]\|_1^2}, \quad (44)$$

880 where the inequality follows from Holder's inequality.

881 For each $i = 1, \dots, n$, we have

$$882 \|A[i]\|_1 = \sum_{S \in 2^{\mathcal{D}}} |A[i, S]| \quad (45)$$

$$883 = \sum_{z=1}^n \sum_{S: C_i \in S, |S|=z} \frac{1}{n} \binom{n-1}{z-1}^{-1} + \sum_{z=0}^{n-1} \sum_{S: C_i \notin S, |S|=z} \frac{1}{n} \binom{n-1}{z}^{-1} \quad (46)$$

$$884 = \sum_{z=1}^n \frac{1}{n} \binom{n-1}{z-1}^{-1} \cdot \binom{n-1}{z-1} + \sum_{z=0}^{n-1} \frac{1}{n} \binom{n-1}{z}^{-1} \cdot \binom{n-1}{z} \quad (47)$$

$$885 = \frac{1}{n} \cdot n + \frac{1}{n} \cdot n = 2, \quad (48)$$

886 where the third equality follows from counting the number of subsets. Hence, we have

$$887 \mathbb{E}[\|\tilde{\beta}_k^{\text{ft}} - \beta^*\|_2] \leq 2\sqrt{n} \cdot \mathbb{E}\|\tilde{v}_k^{\text{ft}} - v^*\|_\infty \quad (49)$$

$$888 = 2\sqrt{n} \cdot \mathbb{E}\left[\max_{S \in 2^{\mathcal{D}}} |\mathcal{F}(\tilde{\theta}_{S,k}^{\text{ft}}) - \mathcal{F}(\theta_S^*)|\right] \quad (50)$$

$$889 \leq 2\sqrt{n} \cdot \left(\mathbb{E}\left[\max_{S \in 2^{\mathcal{D}}} |\mathcal{F}(\tilde{\theta}_{S,k}^{\text{ft}}) - \mathcal{F}(\tilde{\theta}_S^*)|\right] + \mathbb{E}\left[\max_{S \in 2^{\mathcal{D}}} |\mathcal{F}(\tilde{\theta}_S^*) - \mathcal{F}(\theta_S^*)|\right]\right) \quad (51)$$

$$890 = 2\sqrt{n} \cdot \mathbb{E}\left[\max_{S \in 2^{\mathcal{D}}} |\mathcal{F}(\tilde{\theta}_S^*) - \mathcal{F}(\theta_S^*)|\right], \quad (52)$$

as $k \rightarrow \infty$, where the last equality follows the same steps as in Proposition 1. Finally, with the assumption that $\mathbb{E}[\max_{S \in 2^{\mathcal{D}}} |\mathcal{F}(\theta_S^*) - \mathcal{F}(\theta_S^*)|] \leq C$, we have

$$\mathbb{E}[\|\tilde{\beta}_k^{\text{ft}} - \beta^*\|_2] \leq 2\sqrt{n}C. \quad (53)$$

□

B DATASETS AND MODEL PROPERTIES

CIFAR-20 (32 × 32). The full CIFAR-100 dataset⁷ contains 50,000 training samples across 100 classes, with each class labeled by a labeler (Krizhevsky et al., 2009). These labelers were compensated to ensure the removal of initially mislabeled images. For computational feasibility in the LDS evaluations, we follow a similar approach in Zheng et al. (2023) to create a smaller subset, CIFAR-20. This subset includes 10,000 training samples randomly selected from four superclasses in CIFAR-100: "large carnivores", "flowers", "household electrical devices", and "vehicles 1". For Inception Score calculation, we generate 10,240 samples and use Inception Score Pytorch⁸.

CelebA-HQ (256 × 256). The original CelebA-HQ dataset (Karras et al., 2018) comprises of 30,000 face images with 6,217 unique identities. We downloaded a preprocessed dataset from <https://github.com/ndb796/LatentHSJA>, which contain 5,478 images from 307 identities, each with 15 or more images. For our experiment, we randomly sample 50 identities, totaling 895 images. Also, to match the input dimension required by the implementation of latent diffusion model, we resize the original images from a resolution of 1024 × 1024 to 256 × 256. To calculate the diversity score based on Equation (8), we first generate 1,024 samples from the model trained on the full dataset and extract image embeddings using the pretrained BLIP-VQA image encoder⁹ (Li et al., 2022). These embeddings are then clustered into 20 distinct groups as the reference clusters using the Ward linkage criterion (Jh Jr, 1963), representing groups with demographic characteristics. Subsequently, for models trained on various subsets of celebrities, we generate 1,024 samples and assign them into these 20 reference clusters.

ArtBench Post-Impressionism (256 × 256). ArtBench-10 is a dataset for benchmarking artwork generation with 10 art styles, consisting of 5,000 training images per style (Liao et al., 2022). For our experiments, we consider the 5,000 training images corresponding to the art style "post-impressionism" from 258 artists. The aesthetic score predictor¹⁰ is a linear model built on top of CLIP to predict the aesthetic quality of images as a proxy to how much people, on average, perceive an image as aesthetically pleasing.

C ADDITIONAL DETAILS ON TRAINING AND INFERENCE

CIFAR-20 and CelebA-HQ. For CIFAR-20, we follow the original implementation of the unconditional DDPMs (Ho et al., 2020) where the model has 35.7M parameters. For CelebA-HQ, we follow the implementation of LDM (Rombach et al., 2022) with 274M parameters and a pre-trained VQ-VAE (Razavi et al., 2019). For both datasets, the maximum diffusion time step is set to $T = 1000$ during training, with a linear variance schedule for the forward diffusion process ranging from $\beta_1 = 10^{-4}$ to $\beta_T = 0.02$. For both CIFAR-20 and CelebA-HQ, we use the Adam optimizer (Loshchilov & Hutter, 2017) and apply random horizontal flipping as data augmentation. Both the DDPM and LDM are trained for 20,000 steps with a batch size of 64 and a learning rate of 10^{-4} . During inference, images are generated using the 100-step DDIM solver (Song et al., 2020a).

ArtBench (Post-Impressionism). A Stable Diffusion model¹¹ (Rombach et al., 2022) is fine-tuned using LoRA (Hu et al., 2021) with rank = 256, corresponding to 5.1M LoRA parameters. The prompt is set to "a Post-Impressionist painting" for each image. The LoRA parameters are trained using the AdamW optimizer (Loshchilov & Hutter, 2017) with a weight decay of 10^{-6} , for 200 epochs and

⁷<https://www.cs.toronto.edu/~kriz/cifar.html>

⁸<https://github.com/sbarratt/inception-score-pytorch>

⁹<https://huggingface.co/Salesforce/blip-vqa-base>

¹⁰<https://github.com/LAION-AI/aesthetic-predictor>

¹¹<https://huggingface.co/lambdalabs/minisD-diffusers>

a batch size of 64. Cosine learning rate annealing is used, with 500 warm-up steps and an initial learning rate of 3×10^{-4} . At inference time, images are generated using the PNDM scheduler with 100 steps (Karras et al., 2022).

For training diffusion models, we utilize NVIDIA GPUs: RTX 6000, A40, and A100, equipped with 24GB, 48GB, and 80GB of memory, respectively. This study employs the Diffusers package version 0.24.0¹² to train models across. Per-sample gradients are computed using the techniques outlined in the PyTorch package tutorial (version 2.2.1)¹³. Furthermore, we apply the TRAK package¹⁴ to project gradients with a random projection matrix. All experiments are conducted on systems equipped with 64 CPU cores and the specified NVIDIA GPUs.

For CelebA-HQ, we implement two techniques to reduce GPU memory usage during training. First, we pre-compute the embeddings of VQ-VAE for all training samples, since the VQ-VAE is kept frozen during training. This approach allows us to avoid loading the VQ-VAE module into GPU memory during training. Second, we use the 8-bit Adam optimizer implemented in the bitsandbytes Python package (Detmeters et al., 2022).

D EMPIRICAL VERIFICATION OF PROPOSITION 1 AND COROLLARY 1

Proposition 1 suggests that increasing the number of fine-tuning steps can lead to a better approximation of the retrained model property $\mathcal{F}(\theta_{S_j}^*)$ using the sparsified fine-tuned model property $\mathcal{F}(\tilde{\theta}_{S_j,k}^{\text{ft}})$. Here, we empirically measure the similarity between $\mathcal{F}(\theta_{S_j}^*)$ and $\mathcal{F}(\tilde{\theta}_{S_j,k}^{\text{ft}})$, with 100 subsets S_j sampled from the Shapley kernel and varying the number of sparsified fine-tuning steps k . As Proposition 1 provides an upper bound on the estimation error, the possibility of a constant shift should be considered¹⁵. Therefore, we focus on the Pearson correlation between $\{\mathcal{F}(\theta_{S_j}^*)\}_{j=1}^{100}$ and $\{\mathcal{F}(\tilde{\theta}_{S_j,k}^{\text{ft}})\}_{j=1}^{100}$ as the similarity metric. As shown in Figure 5, the approximation generally becomes better with more fine-tuning steps.

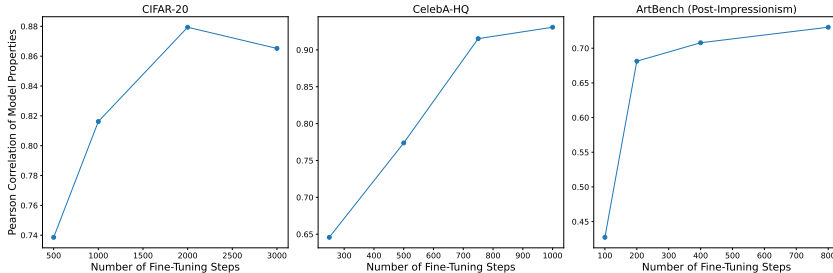


Figure 5: Pearson correlation between model behaviors evaluated with retraining vs. sparsified fine-tuning, with varying number of fine-tuning steps. Models are retrained or fine-tuned on 100 contributor subsets sampled from the Shapley kernel.

Proposition 2 suggests that increasing the number of fine-tuning steps can also lead to a better approximation of the retrained Shapley values (denoted as β^*) using Shapley values estimated through sparsified fine-tuning (denoted as $\tilde{\beta}_k^{\text{ft}}$). Here, we compare the correlation between β^* and $\tilde{\beta}_k^{\text{ft}}$, both estimated with 500 contributor subsets, with varying number of fine-tuning steps k . As shown in Figure 6, the approximation tends to become better with more fine-tuning steps.

Finally, we note there is a trade-off between better approximation and computational efficiency. As shown in Figure 7, average runtime increases linearly with more fine-tuning steps.

¹²<https://pypi.org/project/diffusers/>

¹³<https://pytorch.org/>

¹⁴<https://trak.csail.mit.edu/quickstart>

¹⁵For example, $\mathbb{E}[|\mathcal{F}(\tilde{\theta}_{S_j,k}^{\text{ft}}) - \mathcal{F}(\theta_{S_j}^*)|] \leq B$ still holds when $\mathcal{F}(\tilde{\theta}_{S_j,k}^{\text{ft}}) = \mathcal{F}(\theta_{S_j}^*) + B'$ for some $-B \leq B' \leq B$

1026
1027
1028
1029
1030
1031
1032
1033
1034
1035
1036
1037
1038

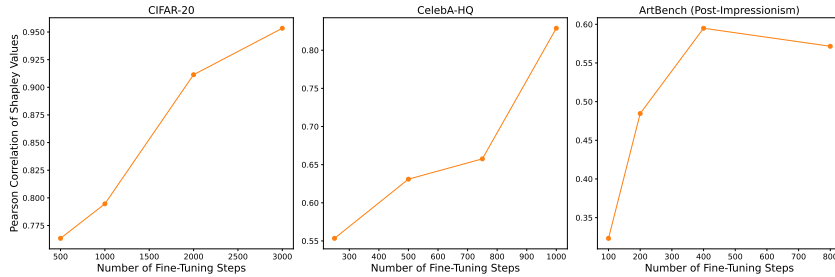


Figure 6: Pearson correlation between the Shapley values estimated with retraining vs. sparsified fine-tuning, with varying number of fine-tuning steps. Shapley values are estimated with 500 contributor subsets sampled from the Shapley kernel.

1039
1040
1041
1042
1043
1044
1045
1046
1047
1048

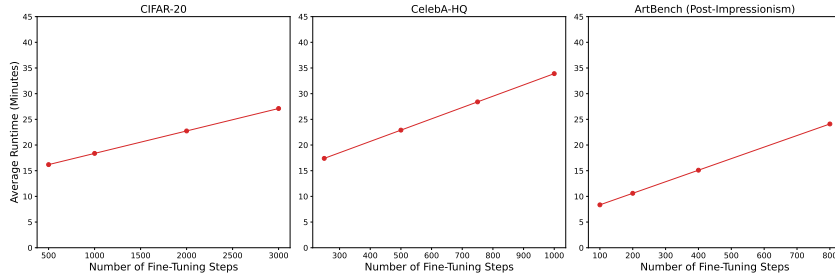


Figure 7: Average runtime of sparsified fine-tuning for the Shapley kernel.

E DATA ATTRIBUTION METHODS FOR DIFFUSION MODELS

1051
1052
1053
1054
1055
1056
1057
1058
1059
1060
1061
1062
1063
1064
1065
1066
1067
1068
1069
1070
1071

Here we provide definitions and implementation details of the baselines used in Section 4. For TRAK-based approaches, we follow the implementation details in Zheng et al. (2023)¹⁶.

Raw pixel similarity. This is a simple baseline that uses each raw image as the representation and then computes the cosine similarity between the generated sample of interest and each training sample as the attribution score.

Embeddings distance. This method computes the l_2 distances between training samples encoded using BLIP-VQA¹⁷ (Li et al., 2022), and the average embedding of each reference cluster as the attribution score.

CLIP similarity. This method utilizes CLIP¹⁸ (Radford et al., 2021) to encode each sample into an embedding and then compute the cosine similarity between the generated sample of interest and each training sample as the attribution score.

Leave-one-out. Leave-one-out (LOO) evaluates the change in model property due to the removal of a single data contributor i from the training set (Koh & Liang, 2017). Formally, it is defined as:

$$\tau_{\text{LOO}}(\mathcal{F}, \mathcal{D})_i = \mathcal{F}(\theta^*) - \mathcal{F}(\theta_{\mathcal{D} \setminus \mathcal{C}_i}^*), \tag{54}$$

where $\mathcal{F}(\theta^*)$ denotes the global property for the model trained with the full dataset, and $\mathcal{F}(\theta_{\mathcal{D} \setminus \mathcal{C}_i}^*)$ represents the global property of the mode trained with the data provided by the i th contributor.

Gradient similarity. This is a gradient-based influence estimator (Charpiat et al., 2019), which computes the cosine similarity using the gradient representations of the generated sample of interest, $\tilde{\mathbf{x}}$ and each training sample $\mathbf{x}^{(j)}$ as the attribution score:

$$\frac{\mathcal{P}^\top \nabla_{\theta} \mathcal{L}_{\text{Simple}}(\mathbf{x}^{(j)}; \theta^*) \cdot \mathcal{P}^\top \nabla_{\theta} \mathcal{L}_{\text{Simple}}(\tilde{\mathbf{x}}; \theta^*)}{\|\mathcal{P}^\top \nabla_{\theta} \mathcal{L}_{\text{Simple}}(\mathbf{x}^{(j)}; \theta^*)\| \|\mathcal{P}^\top \nabla_{\theta} \mathcal{L}_{\text{Simple}}(\tilde{\mathbf{x}}; \theta^*)\|} \tag{55}$$

¹⁶<https://github.com/sail-sg/D-TRAK/>
¹⁷<https://huggingface.co/Salesforce/blip-vqa-base>
¹⁸<https://github.com/openai/CLIP>

TRAK. Park et al. (2023) propose an approach that aims to enhance the efficiency and scalability of data attribution for classifiers. Zheng et al. (2023) adapt TRAK for attributing images generated by diffusion models, defined as follows:

$$\frac{1}{S} \sum_{s=1}^S \Phi_s (\Phi_s^\top \Phi_s + \lambda I)^{-1} \mathcal{P}_s^\top \nabla_{\theta} \mathcal{L}_{\text{Simple}}(\tilde{\mathbf{x}}; \theta_s^*), \text{ and} \quad (56)$$

$$\Phi_s = [\phi_s(\mathbf{x}^{(1)}), \dots, \phi_s(\mathbf{x}^{(N)})]^\top, \text{ where } \phi_s(\mathbf{x}) = \mathcal{P}_s^\top \nabla_{\theta} \mathcal{L}_{\text{Simple}}(\mathbf{x}; \theta_s^*), \quad (57)$$

where $\mathcal{L}_{\text{Simple}}$ is the diffusion loss used during training, \mathcal{P}_s is a random projection matrix, and λI serves for numerical stability and regularization.

D-TRAK. Zheng et al. (2023) find that, compared to the theoretically motivated setting where the loss function is defined as $\mathcal{L} = \mathcal{L}_{\text{Simple}}$, using alternative functions—such as the squared loss $\mathcal{L}_{\text{Square}}$ —to replace both the loss function and local model property result in improved performance:

$$\frac{1}{S} \sum_{s=1}^S \Phi_s (\Phi_s^\top \Phi_s + \lambda I)^{-1} \mathcal{P}_s^\top \nabla_{\theta} \mathcal{L}_{\text{Square}}(\tilde{\mathbf{x}}; \theta_s^*), \text{ and} \quad (58)$$

$$\Phi_s = [\phi_s(\mathbf{x}^{(1)}), \dots, \phi_s(\mathbf{x}^{(N)})]^\top, \text{ where } \phi_s(\mathbf{x}) = \mathcal{P}_s^\top \nabla_{\theta} \mathcal{L}_{\text{Square}}(\mathbf{x}; \theta_s^*). \quad (59)$$

Journey-TRAK. Georgiev et al. (2023) focus on attributing noisy images \mathbf{x}_t during the denoising process. It attributes training data not only for the final generated sample but also for the intermediate noisy samples throughout the denoising process. At each time step, the reconstruction loss is treated as a local model property. Following (Zheng et al., 2023), we compute attribution scores by averaging over the generation time steps, as shown below:

$$\frac{1}{T'} \frac{1}{S} \sum_{t=1}^{T'} \sum_{s=1}^S \Phi_s (\Phi_s^\top \Phi_s + \lambda I)^{-1} \mathcal{P}_s^\top \nabla_{\theta} \mathcal{L}_{\text{Simple}}^t(\tilde{\mathbf{x}}_t; \theta_s^*), \text{ and} \quad (60)$$

$$\Phi_s = [\phi_s(\mathbf{x}^{(1)}), \dots, \phi_s(\mathbf{x}^{(N)})]^\top, \text{ where } \phi_s(\mathbf{x}) = \mathcal{P}_s^\top \nabla_{\theta} \mathcal{L}_{\text{Simple}}(\mathbf{x}; \theta_s^*). \quad (61)$$

Here, $\mathcal{L}_{\text{Simple}}^t$ is the diffusion loss restricted to the time step t (hence without taking the expectation over the time step).

In practice, we follow the main implementation by Zheng et al. (2023) that considers TRAK, D-TRAK, and Journey-TRAK as retraining-free methods. That is, $S = 1$, and $\theta_1^* = \theta^*$ is the original diffusion model trained on the entire dataset.

Relative Influence. Proposed by Barshan et al. (2020), the θ -relative influence functions estimator normalizes the influence functions estimator of Koh & Liang (2017) by the HVP magnitude. Following Zheng et al. (2023), we combine this estimator with TRAK dimension reduction. The attribution for each training sample $\mathbf{x}^{(j)}$ is as follows:

$$\frac{\mathcal{P}^\top \nabla_{\theta} \mathcal{L}_{\text{Simple}}(\tilde{\mathbf{x}}; \theta^*) \cdot (\Phi_{\text{TRAK}}^\top \cdot \Phi_{\text{TRAK}} + \lambda I)^{-1} \cdot \mathcal{P}^\top \nabla_{\theta} \mathcal{L}_{\text{Simple}}(\mathbf{x}^{(j)}; \theta^*)}{\left\| (\Phi_{\text{TRAK}}^\top \cdot \Phi_{\text{TRAK}} + \lambda I)^{-1} \cdot \mathcal{P}^\top \nabla_{\theta} \mathcal{L}_{\text{Simple}}(\mathbf{x}^{(j)}; \theta^*) \right\|}, \quad (62)$$

and

$$\Phi_{\text{TRAK}} = [\phi(\mathbf{x}^{(1)}), \dots, \phi(\mathbf{x}^{(N)})]^\top, \text{ where } \phi(\mathbf{x}) = \mathcal{P}^\top \nabla_{\theta} \mathcal{L}_{\text{Simple}}(\mathbf{x}; \theta^*). \quad (63)$$

Renormalized Influence. Introduced by Hammoudeh & Lowd (2022), this method renormalizes the influence functions by the magnitude of the training sample’s gradients. Similar to relative influence, we made an adaptation following Zheng et al. (2023). The attribution for each training sample $\mathbf{x}^{(j)}$ is as follows:

$$\frac{\mathcal{P}^\top \nabla_{\theta} \mathcal{L}_{\text{Simple}}(\tilde{\mathbf{x}}; \theta^*) \cdot (\Phi_{\text{TRAK}}^\top \cdot \Phi_{\text{TRAK}} + \lambda I)^{-1} \cdot \mathcal{P}^\top \nabla_{\theta} \mathcal{L}_{\text{Simple}}(\mathbf{x}^{(j)}; \theta^*)}{\left\| \mathcal{P}^\top \nabla_{\theta} \mathcal{L}_{\text{Simple}}(\mathbf{x}^{(j)}; \theta^*) \right\|}, \quad (64)$$

1134 and

$$1135 \Phi_{\text{TRAK}} = \left[\phi(\mathbf{x}^{(1)}), \dots, \phi(\mathbf{x}^{(N)}) \right]^\top, \text{ where } \phi(\mathbf{x}) = \mathcal{P}^\top \nabla_{\theta} \mathcal{L}_{\text{Simple}}(\mathbf{x}; \theta^*). \quad (65)$$

1137 For TRAK-based methods and gradient similarity, we compute gradients using the final model
 1138 checkpoint, meaning that $S = 1$ in Equation (56). We select 100 time steps evenly spaced within the
 1139 interval $[1, T]$ for computing the diffusion loss. At each time step, we introduce one instance of noise.
 1140 The projection dimensions are set to $k = 4096$ for CIFAR-20 and $k = 32768$ for CelebA-HQ and
 1141 ArtBench (Post-Impressionism). For D-TRAK, we use the best-performing output function $\mathcal{L}_{\text{Square}}$
 1142 and choose $\lambda = 5e^{-1}$ as in Zheng et al. (2023).

1143 **TracIn.** Pruthi et al. (2020) propose to attribute the training sample’s influence based on first-order
 1144 approximation with saved checkpoints during the training process. However, this is also a major
 1145 limitation because sometimes it is impossible to obtain checkpoints for models such as Stable
 1146 Diffusion (Rombach et al., 2022).

1147
1148
1149
1150
1151
1152
1153
1154
1155
1156
1157
1158
1159
1160
1161
1162
1163
1164
1165
1166
1167
1168
1169
1170
1171
1172
1173
1174
1175
1176
1177
1178
1179
1180
1181
1182
1183
1184
1185
1186
1187

F ADDITIONAL EXPERIMENT RESULTS

In this section, we present additional experiment results, including 1) LDS results across different datamodel alpha and computational budgets, 2) generated images after removing top contributing groups, 3) the performance of alternative unlearning approaches in CIFAR-20, and 4) analysis for top contributors in each dataset.

Table 2: Average runtime for data subset in minutes (training + inference) for Shapley values estimated with retraining, fine-tuning (FT), sparsified FT, and LoRA fine-tuning.

Method	CIFAR-20	CelebA-HQ	ArtBench (Post-Impressionism)
Retrain	77.4 + 20.8	213.4 + 26.5	190.6 + 6.4
FT	6.06 + 18.9	17.5 + 27.0	4.4 + 6.4
Sparsified FT	4.37 + 14.0	11.0 + 11.9	4.5 + 6.1
LoRA	4.21 + 19.0	5.5 + 26.7	-

First, we provide the training cost incurred for each method. Utilizing 8 RTX-6k GPUs, the total runtime cost for sparsified-FT Shapley is under one day for each dataset. In contrast, the corresponding runtime costs for retraining-based Shapley are 4.3 days, 10.4 days, and 17.1 days. This highlights that sparsified-FT Shapley is more computationally feasible than retraining-based Shapley.

F.1 CIFAR-20

Table 3: LDS (%) results with $\alpha = 0.25, 0.5, 0.75$ on CIFAR-20, with the Inception Score of 10,240 generated images as the global model property. Means and 95% confidence intervals across three random initializations are reported.

Method	$\alpha = 0.25$	$\alpha = 0.5$	$\alpha = 0.75$
Pixel similarity (average)	-10.88 ± 9.61	-11.81 ± 4.56	-20.82 ± 5.57
Pixel similarity (max)	-17.42 ± 0.83	-31.80 ± 2.90	-23.88 ± 1.28
CLIP similarity (average)	-0.34 ± 4.65	-21.27 ± 1.37	-13.13 ± 1.96
CLIP similarity (max)	-1.19 ± 15.19	11.31 ± 0.37	16.05 ± 7.30
Gradient similarity (average)	6.48 ± 10.98	5.79 ± 3.67	-10.75 ± 7.06
Gradient similarity (max)	7.22 ± 3.88	-0.89 ± 3.17	-4.82 ± 4.71
Relative IF	1.14 ± 13.51	5.23 ± 5.50	5.21 ± 3.78
Renormalized IF	9.09 ± 13.40	11.39 ± 6.79	7.99 ± 4.02
TRAK	3.62 ± 14.02	7.94 ± 5.67	6.59 ± 3.88
Journey-TRAK	-30.09 ± 3.85	-42.92 ± 2.15	-40.43 ± 3.46
D-TRAK	21.02 ± 6.76	10.90 ± 1.21	21.90 ± 5.02
LOO	17.01 ± 5.29	30.66 ± 6.11	13.64 ± 4.99
Sparsified-FT Shapley (Ours)	51.24 ± 3.39	61.48 ± 2.27	59.15 ± 4.24

Table 4: LDS (%) results on Shapley value with different number of subset S .

α	Method	$S = 100$	$S = 200$	$S = 300$	$S = 400$	$S = 500$
0.25	Retraining	43.88 (3.97)	49.95 (3.20)	57.56 (2.52)	62.68 (1.85)	65.90 (1.52)
	Sparsified-FT	8.46 (13.41)	23.92 (6.27)	33.88 (8.33)	54.88 (7.44)	51.24 (3.39)
	FT	13.57 (7.09)	40.01 (8.30)	28.94 (8.59)	24.58 (6.07)	20.57 (3.02)
	LoRA	12.00 (0.65)	29.61 (1.37)	54.26 (3.38)	51.55 (6.40)	61.60 (7.44)
0.5	Retraining	48.84 (2.00)	39.55 (3.17)	57.24 (2.69)	66.81 (2.99)	70.58 (2.05)
	Sparsified-FT	-5.41 (4.78)	38.00 (3.06)	47.74 (1.49)	63.62 (2.30)	61.48 (2.27)
	FT	13.57 (7.09)	40.01 (8.30)	28.94 (8.59)	24.58 (6.07)	39.60 (3.03)
	LoRA	29.90 (2.96)	41.41 (1.28)	41.27 (0.59)	34.20 (0.53)	30.86 (1.07)
0.75	Retraining	51.39 (3.21)	45.85 (3.99)	61.91 (4.62)	70.59 (3.13)	72.07 (4.83)
	Sparsified-FT	-11.44 (2.26)	33.98 (0.98)	48.16 (5.18)	59.65 (5.34)	59.15 (4.24)
	FT	33.90 (5.88)	26.09 (8.55)	45.49 (6.83)	46.92 (5.96)	38.51 (4.62)
	LoRA	24.55 (2.16)	31.07 (7.83)	32.67 (7.94)	35.01 (7.05)	35.16 (8.14)

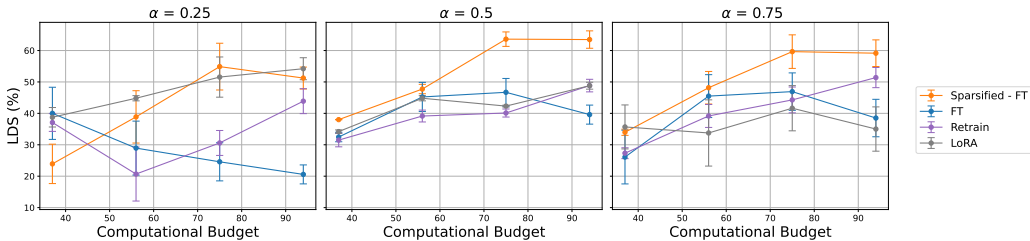


Figure 8: LDS (%) results on CIFAR-20 for Shapley values estimated with sparsified fine-tuning (FT), finet-tuning (FT), LoRA fine-tuning, and retraining under the same computational budgets (1 unit = runtime to retrain and run inference on a full model).

Table 5: LDS (%) results for retraining-based attribution across Shapley, Leave-One-Out (LOO), and Banzhaf distributions with $\alpha = 0.25, 0.5, 0.75$ on CIFAR-20. The global model behavior is evaluated using the Inception Score of 10,240 generated images. Means and 95% confidence intervals across three random initializations are reported. For sparsified fine-tuning (sFT) and fine-tuning (FT), the number of fine-tuning steps is set to 1000.

Method	$\alpha = 0.25$	$\alpha = 0.5$	$\alpha = 0.75$
LOO (retraining)	17.01 \pm 5.29	30.66 \pm 6.11	13.64 \pm 4.99
Banzhaf (retraining)	10.59 \pm 8.64	37.11 \pm 2.33	42.78 \pm 1.85
Shapley (retraining)	65.90 \pm 1.52	70.58 \pm 2.05	72.07 \pm 4.83
LOO (FT)	-55.00 \pm 11.76	-66.06 \pm 2.28	-54.58 \pm 7.02
Banzhaf (FT)	-11.20 \pm 6.42	9.09 \pm 2.67	16.79 \pm 1.12
Shapley (FT)	20.57 \pm 3.02	39.60 \pm 3.03	38.51 \pm 4.62
LOO (sFT)	29.45 \pm 5.96	27.43 \pm 4.20	19.58 \pm 0.35
Banzhaf (sFT)	5.44 \pm 8.59	22.55 \pm 5.07	31.44 \pm 0.27
Shapley (sFT)	51.24 \pm 3.39	61.48 \pm 2.27	59.15 \pm 4.24

1296
 1297
 1298
 1299
 1300
 1301
 1302
 1303
 1304
 1305
 1306
 1307
 1308
 1309
 1310
 1311
 1312
 1313
 1314
 1315
 1316
 1317
 1318
 1319
 1320
 1321
 1322
 1323
 1324
 1325
 1326
 1327
 1328
 1329
 1330
 1331
 1332
 1333
 1334
 1335
 1336
 1337
 1338
 1339
 1340
 1341
 1342
 1343
 1344
 1345
 1346
 1347
 1348
 1349



Figure 9: Inception scores and example images generated with the same initial noises for DDPMs trained without the 10%, 20%, and 40% (top to bottom) most important CIFAR-20 classes based on sparsified-FT Shapley, D-TRAK, and CLIP similarity (max).

F.2 CELEBA-HQ

Table 6: LDS (%) results with $\alpha = 0.25, 0.5, 0.75$ on CelebA-HQ, with the cluster entropy of 1,024 generated images as the global model property. Means and 95% confidence intervals across three random initializations are reported.

Method	$\alpha = 0.25$	$\alpha = 0.5$	$\alpha = 0.75$
Pixel similarity (average)	-1.52 ± 3.14	-8.91 ± 0.93	-4.19 ± 2.25
Pixel similarity (max)	9.53 ± 6.35	21.70 ± 2.05	24.76 ± 0.96
Embedding dist. (average)	3.59 ± 6.47	13.83 ± 1.12	10.89 ± 2.04
Embedding dist. (max)	9.17 ± 2.12	7.32 ± 3.16	22.25 ± 1.87
CLIP similarity (average)	-8.29 ± 4.38	-32.23 ± 0.87	-22.29 ± 2.56
CLIP similarity (max)	-23.62 ± 3.51	-0.93 ± 3.83	-8.86 ± 2.16
Gradient similarity (average)	-19.40 ± 3.81	-18.32 ± 0.65	-21.29 ± 1.76
Gradient similarity (max)	-15.98 ± 2.72	-12.90 ± 1.60	-25.41 ± 2.42
Relative IF	-5.14 ± 2.30	-1.07 ± 0.68	-5.50 ± 1.13
Renormalized IF	-5.27 ± 6.15	10.17 ± 0.57	0.39 ± 1.20
TRAK	-6.59 ± 5.04	3.22 ± 0.75	-3.65 ± 1.24
Journey-TRAK	-16.82 ± 3.25	-2.88 ± 4.02	-12.66 ± 2.27
D-TRAK	-30.77 ± 4.26	-27.23 ± 2.80	-23.67 ± 1.71
LOO	11.9 ± 8.32	-1.22 ± 6.34	-8.47 ± -7.93
Sparsified-FT Shapley (Ours)	10.05 ± 5.33	26.34 ± 3.34	24.08 ± 1.52

Table 7: LDS (%) results on Shapley value with different number of subsets S

α	Method	$S = 100$	$S = 200$	$S = 300$	$S = 400$	$S = 500$
0.25	Retraining	3.54 (0.59)	8.91 (2.61)	16.77 (4.75)	15.58 (6.23)	31.52 (5.56)
	Sparsified - FT	9.95 (5.77)	15.93 (6.29)	9.90 (8.17)	16.12 (6.40)	10.05 (5.33)
	FT	-10.52 (4.26)	2.77 (5.79)	12.29 (4.50)	9.86 (4.84)	13.91 (3.91)
	LoRA	3.07 (1.17)	19.03 (9.47)	26.20 (9.73)	27.17 (7.72)	31.09 (7.72)
0.5	Retraining	19.01 (1.60)	28.43 (2.71)	35.06 (3.48)	23.48 (2.95)	28.58 (3.91)
	Sparsified - FT	20.73 (2.89)	26.83 (3.96)	12.71 (2.06)	27.23 (2.94)	26.34 (3.42)
	FT	1.82 (3.36)	9.25 (2.59)	12.17 (2.83)	8.63 (0.52)	13.77 (1.42)
	LoRA	10.66 (3.56)	20.12 (2.72)	13.99 (1.13)	21.12 (0.85)	22.37 (0.82)
0.75	Retraining	21.14 (0.93)	26.29 (1.37)	31.87 (2.85)	31.60 (2.23)	32.26 (2.08)
	Sparsified - FT	16.05 (0.31)	29.35 (1.43)	9.49 (2.03)	17.70 (1.30)	24.08 (1.52)
	FT	-11.02 (1.51)	-12.07 (4.30)	1.93 (4.82)	0.96 (4.16)	7.37 (3.79)
	LoRA	6.05 (1.17)	9.66 (1.43)	-1.92 (0.77)	9.00 (2.18)	14.60 (2.33)

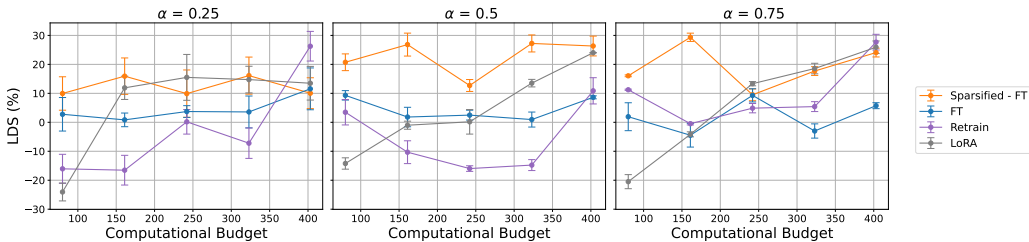


Figure 10: LDS (%) results on CelebA-HQ for Shapley values estimated with sparsified fine-tuning (FT), fine-tuning (FT), and retraining under the same computational budgets (1 unit = runtime to retrain and run inference on a full model).

1404
 1405
 1406
 1407
 1408
 1409
 1410
 1411
 1412
 1413
 1414
 1415
 1416
 1417
 1418
 1419
 1420
 1421
 1422
 1423
 1424
 1425
 1426
 1427
 1428
 1429
 1430
 1431
 1432
 1433
 1434
 1435
 1436
 1437
 1438
 1439
 1440
 1441
 1442
 1443
 1444
 1445
 1446
 1447
 1448
 1449
 1450
 1451
 1452
 1453
 1454
 1455
 1456
 1457

Table 8: LDS (%) results for retraining-based attribution across Shapley, Leave-One-Out (LOO), and Banzhaf distributions with $\alpha = 0.25, 0.5, 0.75$. The global model behavior is calculated with the cluster entropy of 1,024 generated images. Means and 95% confidence intervals across three random initializations are reported. For sparsified fine-tuning (sFT) and fine-tuning (FT), the number of training steps is set to 500.

Method	$\alpha = 0.25$	$\alpha = 0.5$	$\alpha = 0.75$
LOO (retraining)	11.90 ± 8.32	-1.22 ± 6.34	-8.20 ± 0.27
Banzhaf (retraining)	7.87 ± 1.31	6.79 ± 1.27	12.54 ± 2.60
Shapley (retraining)	31.52 ± 5.56	28.58 ± 3.91	32.26 ± 2.08
LOO (FT)	-2.70 ± 1.84	-10.15 ± 1.12	-10.09 ± 1.70
Banzhaf (FT)	1.50 ± 7.36	-2.78 ± 0.69	3.23 ± 1.91
Shapley (FT)	13.91 ± 3.91	13.77 ± 1.42	7.37 ± 3.79
LOO (sFT)	0.93 ± 2.83	-9.26 ± 0.39	-18.80 ± 1.28
Banzhaf (sFT)	7.87 ± 1.31	6.79 ± 1.27	12.54 ± 2.60
Shapley (sFT)	10.05 ± 5.33	26.34 ± 3.34	24.08 ± 1.52

F.3 ARTBENCH (POST-IMPRESSIONISM)

Table 9: LDS (%) results with $\alpha = 0.25, 0.5, 0.75$ on ArtBench (Post-Impressionism), with the 90th percentile of aesthetic scores for 50 generated images as the global model property. Means and 95% confidence intervals across three random initializations are reported.

Method	$\alpha = 0.25$	$\alpha = 0.5$	$\alpha = 0.75$
Pixel similarity (average)	16.57 (3.16)	11.24 (0.63)	-1.19 (5.71)
Pixel similarity (max)	16.62 (2.95)	14.61 (2.72)	3.43 (10.57)
CLIP similarity (average)	-6.03 (1.61)	-6.96 (4.08)	-9.27 (2.74)
CLIP similarity (max)	8.94 (0.43)	-1.75 (4.07)	-1.70 (9.89)
Grad similarity (average)	4.14 (5.14)	0.25 (1.18)	-7.81 (0.89)
Grad similarity (max)	22.10 (9.02)	10.48 (3.11)	1.32 (4.19)
Aesthetic score (average)	24.81 (3.00)	24.85 (2.30)	13.21 (7.82)
Aesthetic score (max)	31.73 (3.04)	21.36 (3.70)	7.45 (11.66)
Relative IF	3.30 (4.98)	-5.02 (1.77)	-3.77 (12.05)
Renormalized IF	-1.71 (4.37)	-11.41 (0.93)	-8.96 (12.86)
TRAK	-0.85 (4.74)	-8.18 (1.30)	-6.78 (13.37)
Journey-TRAK	-14.10 (5.09)	-11.41 (4.22)	-6.83 (2.80)
D-TRAK	19.37 (3.29)	11.30 (3.47)	17.72 (6.87)
Sparsified-FT Shapley (Ours)	52.83 (3.58)	61.44 (2.04)	32.24 (10.93)

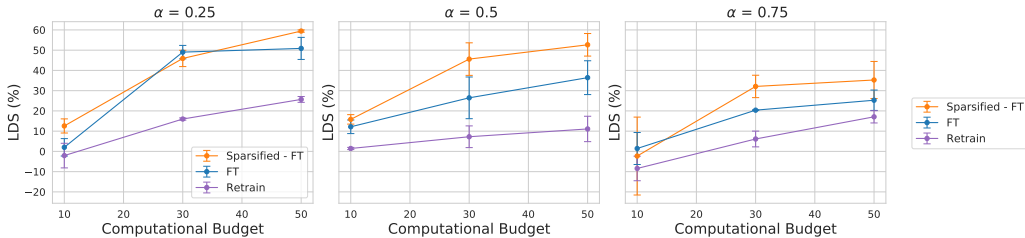


Figure 11: LDS (%) results with $\alpha = 0.25, 0.5, 0.75$ on ArtBench (Post-Impressionism) for Shapley values estimated with sparsified fine-tuning (FT), fine-tuning (FT), and retraining under the same computational budgets (1 unit = runtime to retrain and run inference on a full model).

Table 10: Aesthetic Score (90th percentile of 50 generated images) as the global model behavior. 100 datamodel subsets with alpha = 0.25, 0.5, 0.75 are used for evaluation. Means and 95% confidence intervals across three random initializations are reported. All Shapley values are estimated with 1,000 subsets.

α	Retrain	Sparsified - FT	FT
0.25	53.25 (6.75)	51.15 (7.54)	52.83 (3.58)
0.50	52.30 (2.32)	51.61 (3.21)	61.44 (2.04)
0.75	23.78 (14.07)	33.77 (6.65)	32.24 (10.93)

1512
 1513
 1514
 1515
 1516
 1517
 1518
 1519
 1520
 1521
 1522
 1523
 1524
 1525
 1526
 1527
 1528
 1529
 1530
 1531
 1532
 1533
 1534
 1535
 1536
 1537
 1538
 1539
 1540
 1541
 1542
 1543
 1544
 1545
 1546
 1547
 1548
 1549
 1550
 1551
 1552
 1553
 1554
 1555
 1556
 1557
 1558
 1559
 1560
 1561
 1562
 1563
 1564
 1565

Table 11: LDS (%) results with $\alpha = 0.25, 0.5, 0.75$ on ArtBench (Post-Impressionism), with the 90th percentile of aesthetic score for 50 generated images as the global model property. Means and 95% confidence intervals across three random initializations are reported. For sparsified fine-tuning (sFT) and fine-tuning (FT), the number of fine-tuning steps is set to 200. For Banzhaf and Shapley values, 1000 sbuses are used for estimation.

Method	$\alpha = 0.25$	$\alpha = 0.5$	$\alpha = 0.75$
LOO (retraining)	2.69 ± 4.57	3.74 ± 8.00	-1.13 ± 15.78
Banzhaf (retraining)	4.70 ± 7.28	16.19 ± 1.98	-10.16 ± 9.49
Shapley (retraining)	53.25 ± 6.75	52.30 ± 2.32	23.78 ± 14.07
LOO (FT)	-14.13 ± 5.36	-0.84 ± 1.44	6.62 ± 6.72
Banzhaf (FT)	3.55 ± 6.99	15.30 ± 2.09	-10.79 ± 9.40
Shapley (FT)	52.83 ± 3.58	61.44 ± 2.04	32.24 ± 10.93
LOO (sFT)	2.94 ± 2.64	2.84 ± 7.33	1.00 ± 4.45
Banzhaf (sFT)	3.81 ± 7.16	15.51 ± 2.15	-10.43 ± 9.16
Shapley (sFT)	51.15 ± 7.54	51.61 ± 3.21	33.77 ± 6.65

1566
1567
1568
1569
1570
1571
1572
1573
1574
1575
1576
1577
1578
1579
1580
1581
1582
1583
1584
1585
1586
1587
1588
1589
1590
1591
1592
1593
1594
1595
1596
1597
1598
1599
1600
1601
1602
1603
1604
1605
1606
1607
1608
1609
1610
1611
1612
1613
1614
1615
1616
1617
1618
1619



Figure 12: Two generated images above and two generated images below the 90th percentile of aesthetic scores, for Stable Diffusion models LoRA-finetuned without the top 40% most important artists based on D-TRAK, pixel similarity (max), training image aesthetic score (average), and sparsified-FT Shapley.

1620
1621
1622
1623
1624
1625
1626
1627
1628
1629
1630
1631
1632
1633
1634
1635
1636
1637
1638
1639
1640
1641
1642
1643
1644
1645
1646
1647
1648
1649
1650
1651
1652
1653
1654
1655
1656
1657
1658
1659
1660
1661
1662
1663
1664
1665
1666
1667
1668
1669
1670
1671
1672
1673

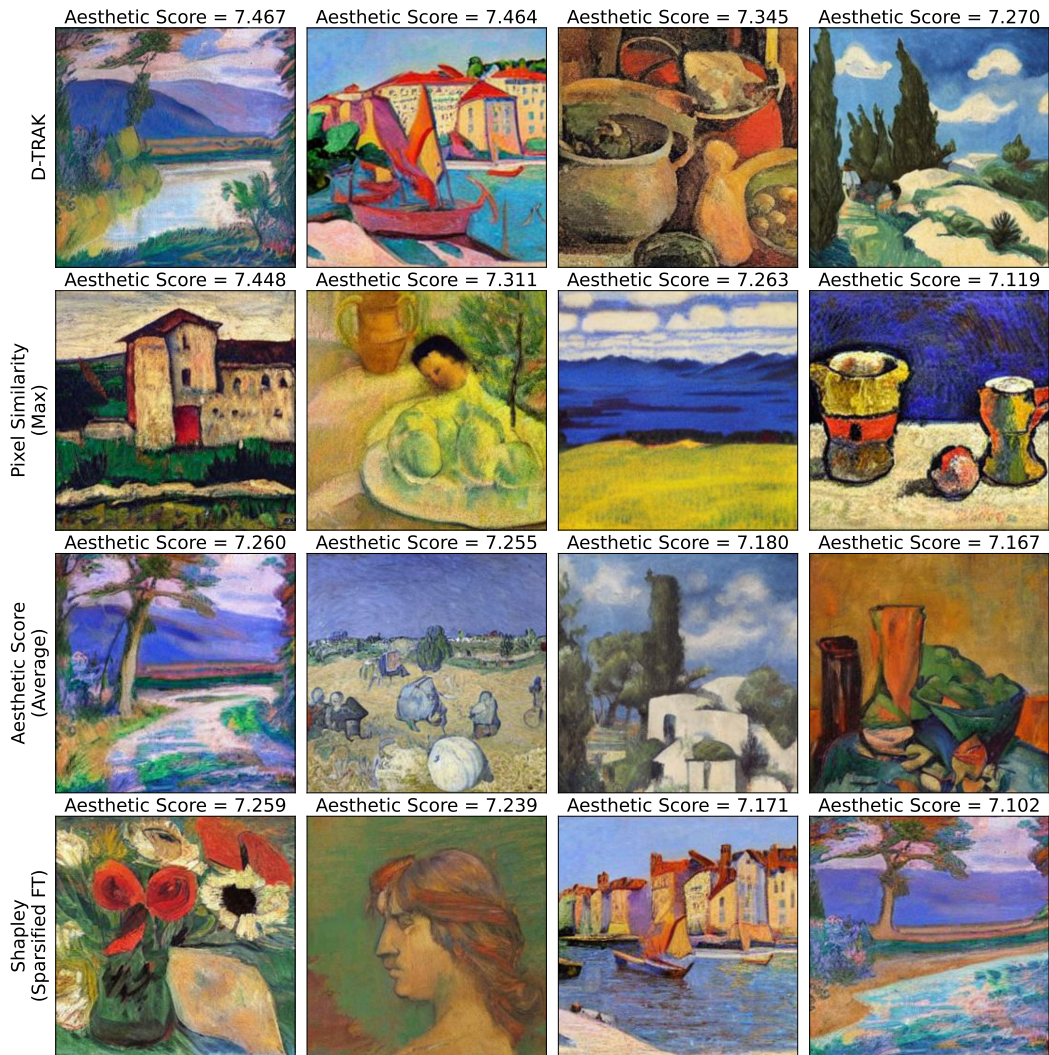


Figure 13: Two generated images above and two generated images below the 90th percentile of aesthetic scores, for Stable Diffusion models LoRA-finetuned without the top 40% most important artists based on D-TRAK, pixel similarity (max), training image aesthetic score (average), and sparsified-FT Shapley.

F.4 ALTERNATIVE UNLEARNING APPROACHES FOR REMOVAL

In this section, we present the performance of unlearning approaches: fine-tuning (FT), gradient ascent (GA) Graves et al. (2021), and influence unlearning (IU) Izzo et al. (2021). To evaluate how well these approaches approximate retraining, we randomly selected 100 subsets from the Shapley sampling distribution, and we computed the FID score between the samples generated by the model retrained on each subset vs. models undergone by the unlearning methods. The resulting average FID scores are 25.5, 185.9, and 101.3 for sparsified fine-tuning (FT), sparsified GA, and sparsified IU, respectively (Table 12). In contrast, the average FID scores without sparsification are 43.1, 145.2, and 67.7 for fine-tuning (FT), GA, and IU, respectively (Table 12). These results indicate that while both GA and IU can effectively unlearn the target set, they significantly degrade overall image quality, Figure 14 and Figure 15. In contrast, sparsified FT demonstrates superior performance, producing better image quality than both GA and IU.

Table 12: FID scores between generated samples from different unlearning approximations and retrained models. Means and 95% confidence intervals across 100 random sampled subsets from Shapley distribution are reported.

Unlearning Method	FID Score
With Sparsification	
Fine-Tuning (FT)	25.5 ± 10.5
Gradient Ascent (GA)	185.9 ± 45.7
Influence Unlearning (IU)	101.3 ± 32.1
Without Sparsification	
Fine-Tuning (FT)	43.1 ± 10.9
Gradient Ascent (GA)	145.2 ± 15.4
Influence Unlearning (IU)	67.7 ± 15.9

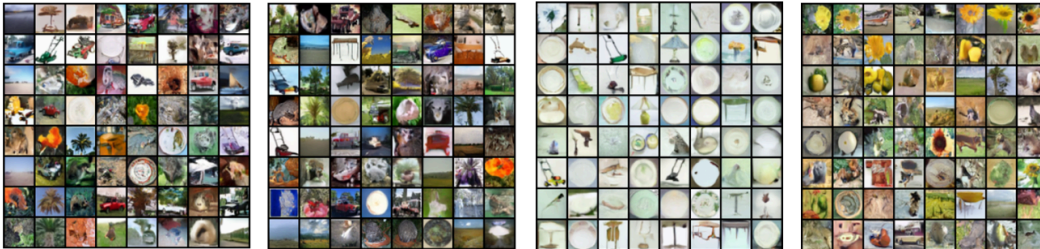


Figure 14: Sample images generated using various unlearning approaches on CIFAR-20 with identical noise inputs: retraining, sparsified fine-tuning (FT), sparsified gradient ascent (GA), and sparsified influence unlearning (IU) (from left to right).

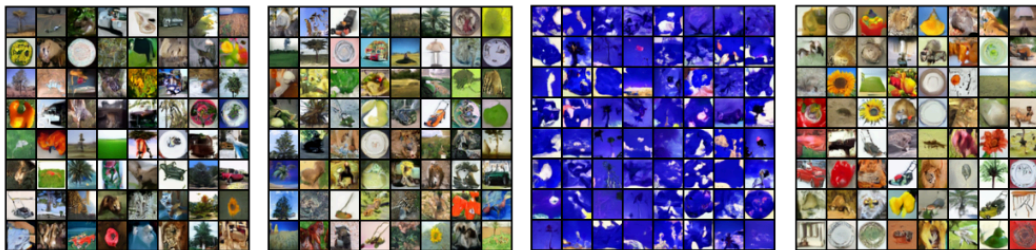


Figure 15: Sample images generated using various unlearning approaches on CIFAR-20 with identical noise inputs: retraining, fine-tuning (FT), gradient ascent (GA), and influence unlearning (IU) (from left to right).

F.5 ANALYSIS OF TOP CONTRIBUTORS

Here, we present an additional analysis of the top contributors identified by sparsified FT. For CIFAR-20, we compute the entropy of the training images for each class based on the softmax outputs of InceptionNet. In the case of CelebA-HQ, the top contributors are predominantly drawn from non-majority clusters.

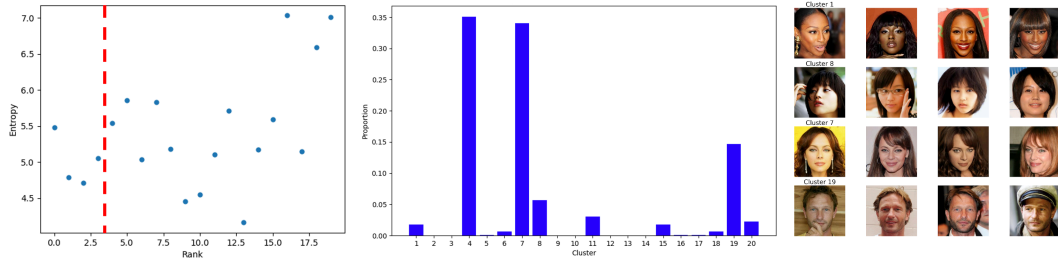


Figure 16: Entropy of each class in CIFAR-20 (left), redline indicates top 20% groups; Distribution of the demographic clusters in the CelebA-HQ dataset (middle). Top 4 celebrity identities by sparsified-FT Shapley (right).

F.6 DATA QUALITY DISTRIBUTION

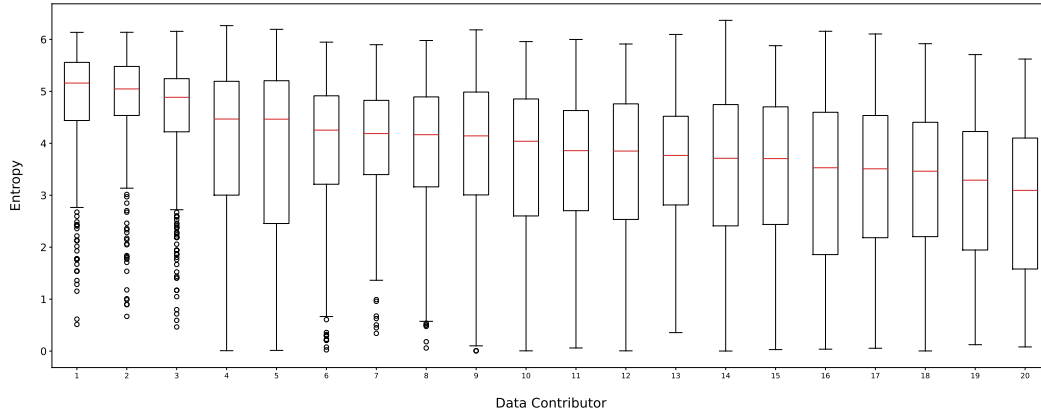


Figure 17: Entropy distributions across data contributors in CIFAR-20.

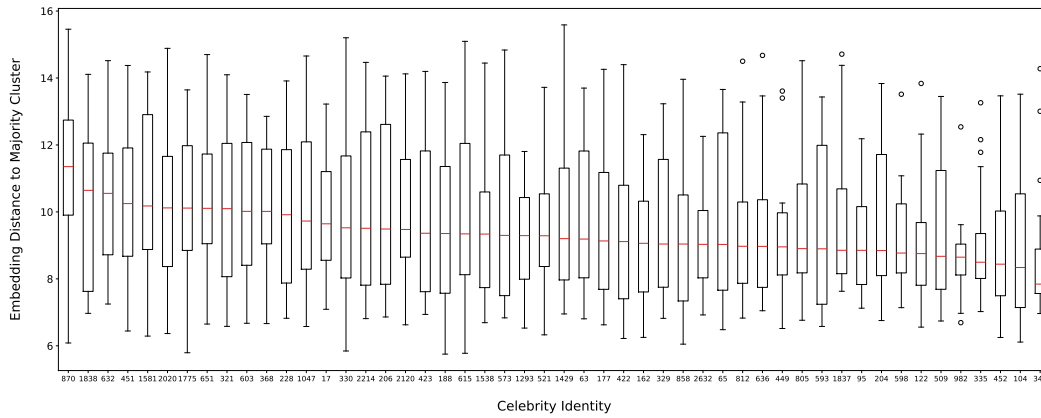


Figure 18: Distributions of embedding distance to the average of majority clusters across celebrity identities in CelebA-HQ.

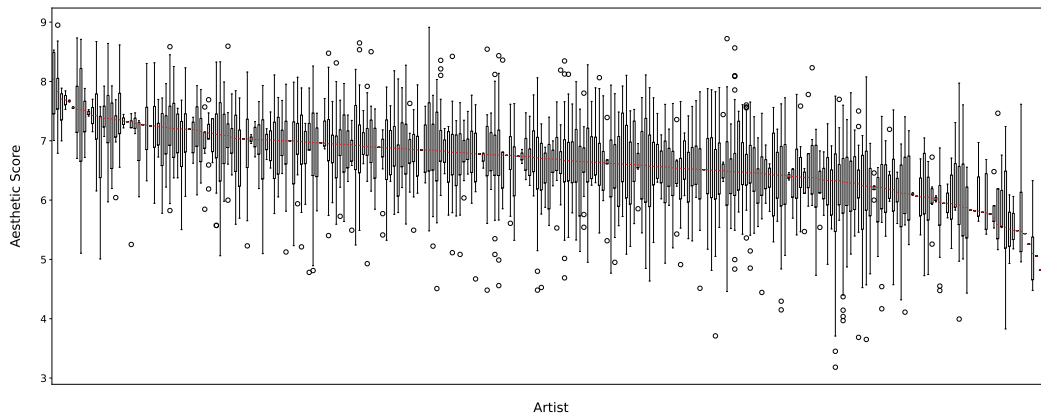


Figure 19: Distributions of aesthetic score across artists in ArtBench (Post-Impressionism).